Interacting rhythms enhance sensitivity of target detection in a fronto-parietal computational model of visual attention

Amélie Aussel[1,2*], **Ian C. Fiebelkorn**[3,4], **Sabine Kastner**[4,5], **Nancy J. Kopell**[1,2†], **Benjamin R. Pittman-Polletta**[1,2†]

***For correspondence:** aaussel@bu.edu (AA)

[†]Supervising author

[1]Cognitive Rhythms Collaborative, Boston University; [2]Department of Mathematics and Statistics, Boston University; [3]Department of Neuroscience and Del Monte Institute for Neuroscience, University of Rochester Medical Center, University of Rochester; [4]Princeton Neuroscience Institute, Princeton University; [5]Department of Psychology, Princeton University

Abstract Even during sustained attention, enhanced processing of attended stimuli waxes and wanes rhythmically, with periods of enhanced and relatively diminished visual processing (and hit rates) alternating at 4 or 8 Hz in a sustained visual attention task. These alternating attentional states occur alongside alternating dynamical states, in which lateral intraparietal cortex (LIP), the frontal eye field (FEF), and the mediodorsal pulvinar exhibit different activity and connectivity at α, β, and γ frequencies – rhythms associated with visual processing, working memory, and motor suppression. To assess whether and how these multiple interacting rhythms contribute to periodicity in attention, we propose a detailed computational model of FEF and LIP that reproduces the rhythmic dynamics and behavioral consequences of observed attentional states, when driven by θ-rhythmic inputs simulating experimentally-observed pulvinar activity. This model reveals that the frequencies and mechanisms of the observed rhythms optimize sensitivity in visual target detection while maintaining functional flexibility.

Introduction

The term 'selective attention' refers broadly to a set of neural mechanisms that are tailored to boost the processing of behaviorally relevant stimuli, allocating the brain's limited processing capacity in an efficient way. Classically, it has been assumed that attention-related modulation of sensory processing is continuous over time during attentional deployment. However, there is now mounting evidence showing that, even during sustained attention, the attentional enhancement of visual processing waxes and wanes over time (***Benedetto et al., 2020***; ***Fiebelkorn and Kastner, 2019b***). In a sustained visual attention task, periods of enhanced sensory processing at an attended location alternate with periods of relatively diminished sensory processing, at a rate of 4–8 cycles per second (i.e., in the θ frequency range) (***Fiebelkorn and Kastner, 2019b***).

This rhythmic sampling of the visual environment is apparent at the behavioral level: measuring the success of target detection as a function of the interval between presentation of a spatially predictive cue and a target reveals an oscillation in hit rates with 8 Hz periodicity at the cued location and 4 Hz periodicity at the uncued location (***Fiebelkorn et al., 2018***, ***2013***; ***Landau***

and Fries, 2012; *Song et al., 2014*; *VanRullen et al., 2007*). Monkey and human electrophysiology has linked this rhythmicity in spatial attention to neural activity in various nodes of the attention network (*Fiebelkorn et al., 2018*, *2019*; *Gaillard et al., 2020*; *Helfrich et al., 2018*). Recordings from the frontal eye field (FEF) and lateral intraparietal area (LIP) in monkeys have revealed that θ-rhythmic changes in behavioral performance are associated with θ phase-dependent attentional states, which alternate at 4 Hz and are characterized by distinct neural dynamics and distinct patterns of functional connectivity between these areas (*Fiebelkorn et al., 2018*, *2019*). These alternating states are also characterized by differences in thalamo-cortical interactions, with the pulvinar – a higher order thalamic nucleus associated with cognitive functions including attention (*Halassa and Kastner, 2017*; *Fiebelkorn and Kastner, 2019a*; *Kastner et al., 2020*; *Saalmann and Kastner, 2011*) and interconnected with the cortical nodes of the attention network (including LIP and FEF) in monkeys (*Gutierrez et al., 2000*; *Romanski et al., 1997*; *Selemon and Goldman-Rakic, 1988*) – specifically coordinating cortical activity during the θ phase associated with enhanced perceptual sensitivity (the "good θ phase"), but not during the θ phase associated with relatively diminished perceptual sensitivity (the "poor θ phase") (*Fiebelkorn et al., 2019*).

The differences in circuit dynamics and connectivity observed during the good and poor θ phases suggest that, even during sustained attentional deployment, the attention system alternates between two states subserving different functional roles. Besides directing attention-related boosts in sensory processing, the attention network also coordinates orienting movements of the body (e.g., head movements) and eyes (e.g., saccadic eye movements) (*Corbetta et al., 1998*; *Moore and Fallah, 2001*). *Fiebelkorn and Kastner* (*2019b*) have proposed that rhythmic sampling reflects the temporal coordination of these sensory and motor functions, helping to avoid potential functional conflicts. That is, periodic dips in perceptual sensitivity (i.e., during the poor θ phase) may be associated with windows of opportunity for the motor system, during which it is easier to shift attention from the presently attended location to another location. Rhythmic sampling may thus provide critical cognitive flexibility, preventing excessive attention to any single stimulus in the environment.

Despite the appeal of this hypothesis, the neuronal circuit mechanisms that underlie the alternating dynamical and attentional states observed during sustained attention remain unknown – as does whether and how their mechanisms contribute to the suppression and enhancement of sensory processing and motor execution. While the good θ phase is characterized by a parietal-driven increase in γ-band activity and a frontal-driven increase in β_2-band activity, the poor θ phase is characterized by increased parietal β_1-band activity (*Fiebelkorn et al., 2018*, *2019*). Whereas γ-band activity has often been associated with enhanced sensory processing (*Fries, 2009*), β_2-band activity has often been associated with the suppression of motor processing (*Gregoriou et al., 2012*; *Pogosyan et al., 2009*; *Zhang et al., 2008*). Consistent with these functional interpretations, during rhythmic sampling, γ-band activity is linked to visual neurons (i.e., neurons that respond to visual stimulation but demonstrate no saccade-related activity), while β-band activity is linked to visual-movement neurons (i.e., neurons that both respond to visual stimulation and demonstrate saccade-related activity) (*Fiebelkorn et al., 2018*). Circuit mechanisms associated with these rhythms have been implicated in sensory processing, attention, and working memory (*Kramer et al., 2008*; *Gelastopoulos et al., 2019*; *Lee et al., 2013*), but whether these mechanisms play a role in the complex rhythmic dynamics of the visual attention network is not known. In this study, we sought to leverage detailed information about neural dynamics during rhythmic sampling as well as insights from previous computational models to address the following questions: What are the mechanisms that generate the γ, β_2, and β_1 oscillations observed in LIP and FEF, and how do these mechanisms and oscillations interact? How is this oscillatory activity flexibly controlled to vary with the θ rhythm, and how does it contribute to function? In particular, can FEF and LIP oscillations explain the variation in behavioral performance over the θ cycle? Finally, are the specific frequencies observed in FEF and LIP, and the θ-frequency timing of these alternating attentional states, functionally significant?

To address these questions, we propose a computational model of FEF and LIP during a sustained attention task. This model, constructed from biologically detailed neurons and consistent with the known anatomy, physiology, and function of frontal and parietal circuits (see Discussion), replicates the γ, β_2, and β_1 activity observed experimentally. It offers an explanation for the frequency-specific causal interactions between LIP and FEF, suggesting a progression during enhanced stimulus processing in which pulvinar input activates FEF and prepares LIP to respond, but top-down β_2 input from FEF is necessary to elicit a γ-rhythmic response from LIP. The model also replicates behavioral results, unexpectedly revealing how an 8 Hz behavioral oscillation (at the cued location) can arise from a 4 Hz alternation of attentional states, in dependence on the strength of connectivity from LIP to FEF. We find that altering the frequency of the underlying θ rhythm, or of the higher-frequency FEF or LIP oscillations, results in decreased model performance, providing evidence for the functional significance of these rhythmic dynamics. Finally, we find that model performance is robust to some changes in model parameters, while other parameter changes produce distinct dynamics – characterized by different rhythms – which we suggest may represent other functional states of FEF and LIP. Thus, our results demonstrate the computational advantages of biologically realistic rhythmic network dynamics, suggesting that they enable attentional networks to participate in attentional, motor, and cognitive tasks with sensitivity, flexibility, and versatility.

Results

We model LIP and FEF activity during a sustained attention task based on the Egly-Driver task (***Fiebelkorn et al.*** (***2019***), see Figure 1-A). In this task, the participant (e.g., monkey) must release a lever when they detect a near-threshold contrast change in a visual scene. A trial begins when the participant fixates on the center of a screen and holds down a lever, and is presented with two horizontal bars. After a short delay, a visual cue appears at the end of one of the bars. The target has a 78% chance of appearing at the same location as the cue, and an 11% chance of appearing at one of the two bar ends adjacent to the cued location (locations A and C in Figure 1-A). After another delay of random duration lasting between 0.3s and 1.6s, the target appears in the form of a near-threshold change in contrast at the end of one of the bars, lasting 0.1s. If the monkey successfully detects the target, it then releases the lever to receive a reward. Hit rates for this task can be analyzed as a function of the time of target presentation (relative to cue presentation), and are found to exhibit θ-band periodicity, with alternating "good" and "poor" θ phases associated with increased and decreased hit rates, respectively, appearing at 4Hz for the uncued object and 8Hz for the cued object (***Fiebelkorn et al., 2013***, ***2019***).

Three of the different brain regions involved in the task, the Frontal Eye Field (FEF), the Lateral Intraparietal area (LIP) and the medio-dorsal pulvinar (mdPul), show distinct patterns of activity between the good and poor θ phases (see Figure 1-B). During the good θ phase, power spectra, Granger causality, spike-field coherence, and cross-frequency coupling indicate that: mdPul provides α-rhythmic (10-15Hz) drive to FEF and LIP; FEF generates β_2 oscillations (20-30Hz) that drive LIP; and LIP generates γ oscillations (>30Hz) that drive FEF. During the poor θ phase, LIP produces β_1 oscillations, which are Granger causal to activity in mdPul and FEF, even though these regions do not exhibit robust activity at any specific frequency during the poor θ phase (***Fiebelkorn et al., 2019***).

Figure 2 shows the basic anatomy of the model. For LIP, we use a laminar model motivated by previous works on attention and memory whose dynamic repertoire of β_1, β_2, and γ rhythms depends on the separation and interaction of lamina-specific physiological properties. A superficial and deep layer can coordinate to produce a β_1 rhythm, while an input layer is used to generate a γ and propagate it to the superficial layer. There are (at least) three different functional classes of pyramidal cells in FEF typically classified based on their sensory- and saccade-related response profiles. In the context of the Egly-Driver task, neurons classified as "visual cells" increase their firing rate when the cue is presented, but not the target; "motor cells" increase their firing rate

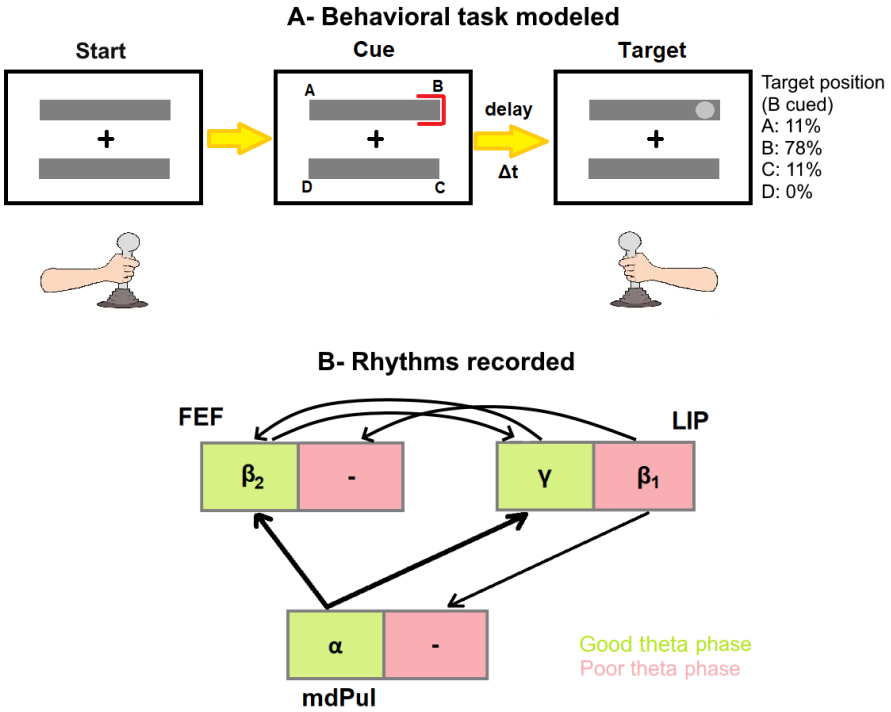

Figure 1. **A- Schematic of the Egly-driver task modeled. B- Neuronal rhythms experimentally measured in FEF, LIP and mdPul during the task.**

when the target is presented but not the cue; and "visuo-motor cells" increase their firing rate when both the cue and the target are presented (***Fiebelkorn et al., 2019***). Thus, FEF is modeled with three different functional modules, a visual module, a visuo-motor module, and a motor module. However, we remain agnostic about the relationships of these functional modules to the laminar structure of FEF, since the geometry of FEF complicates laminar recording and, thus, the laminar properties of FEF rhythms are not clear.

All cell types are modeled as Hodgkin-Huxley point neurons, with spiking (i.e. leak, sodium, and potassium) currents tailored with cell type-specific parameters. In addition to two types of pyramidal cells (granular and superficial regular-spiking (RS) and deep intrinsic bursting (IB)), we model three types of interneurons. Parvalbumin positive interneurons are modeled as fast spiking (FS), and produce fast decaying inhibition (with a timescale of $5ms$), capable of pacing γ oscillations in networks consisting of interacting FS and RS cells. Somatostatin positive (SOM) interneurons contain an h-current in addition to the spiking current, and produce slower decaying inhibition (with a timescale of $20ms$), leading to β_2 oscillations when interacting with RS cells. Finally, vasoactive intestinal peptide (VIP) interneurons are modeled with a potassium D-current, and produce inhibition with a similar decay time to SOM cells, but spike in response to much lower levels of excitation (in accordance with experimental data, ***Tremblay et al.*** (***2016***)). VIP inhibition exclusively targets SOM interneurons in our model (see Section Methods).

All neurons in the model receive tonic excitation at cell type-specific levels, encapsulating the effects of cell type-specific resting membrane potentials and/or background inputs (that do not vary with θ phase) from other brain regions. Each cell also receives some random, gaussian-like excitation, and is initiated with a random membrane potential close to its resting potential. Certain cell types also receive simulated input, designed to match mdPul drive during the task. When isolated modules were analyzed, we substituted simulated inputs for the inputs that would arise from connected modules, based on the dynamics of those modules.

In Section Mechanisms of FEF and LIP oscillations during the cue-target interval, we discuss model behavior during the cue-target interval and show that, when driven by θ-rhythmic inputs

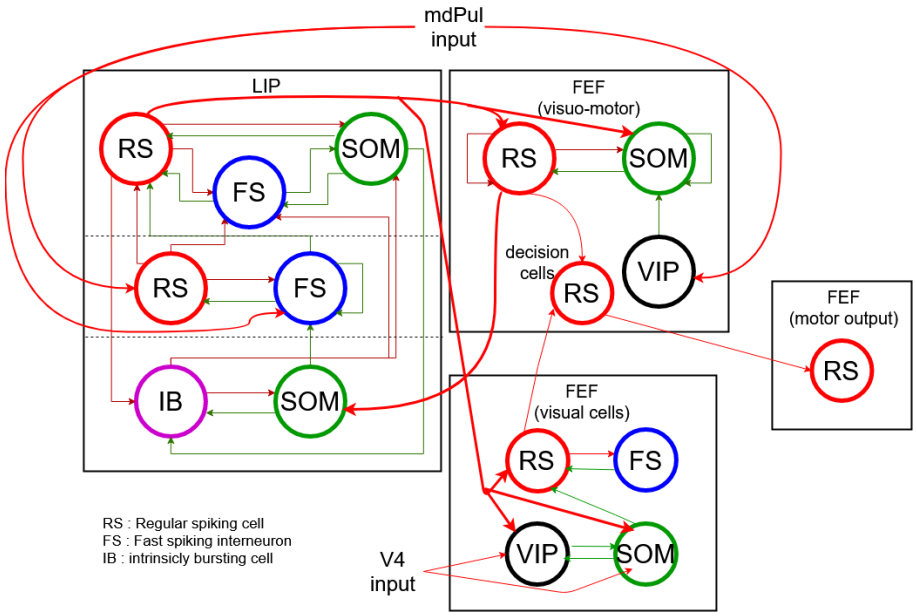

Figure 2. **Diagram of the full LIP and FEF model.**

from mdPul and V4, the model reproduces the rhythms experimentally observed in LIP and FEF during both good and poor θ phases. In Section Mechanisms of target detection, we discuss model behavior on target presentation and show how the FEF model enables enhanced sensitivity and discrimination in target detection. In Section Task performance, we give results about functional implications of the model, and show the importance of the rhythms it generates. Finally, in Section Model robustness and flexibility, we discuss how parameters affect the model behavior, allowing it to exhibit different rhythms and possibly different functional states.

Mechanisms of FEF and LIP oscillations during the cue-target interval

To model the period between cue and target presentation in the modified Egly-Driver task (***Fiebelkorn et al., 2013***), we introduce simulated mdPul input – consisting of bursts of α frequency (12 Hz) excitation arriving during half of each period of a (4 Hz) θ rhythm – targeting LIP granular layer RS and FS cells, and FEF visuo-motor VIP cells. Under these conditions, the model reproduces the nested rhythmic dynamics observed experimentally (Figure 3-B): during mdPul excitation (the putative good θ phase), FEF visuo-motor cells produce a β_2 rhythm, and LIP produces a γ rhythm; during mdPul quiescence (the putative poor θ phase), LIP produces a β_1 rhythm. Note that in the absence of additional visual input to FEF visual cells (i.e., when no target is present on screen), these cells and FEF decision cells are relatively quiet. Below, we explain the circuit mechanisms of these rhythms and their interactions in detail for each module.

LIP module produces β_1 oscillations through period concatenation, and γ oscillations when stimulated by FEF and mdPul

The LIP module (see Figure 4-A) combines two previous laminar models of working memory and attention (***Kramer et al., 2008***; ***Lee et al., 2013***). The first of these is a model of a β_1 rhythm observed in rodent parietal slices (***Kramer et al., 2008***), shown to be useful for retention and manipulation of cell assemblies after the fading of a sensory input (***Gelastopoulos et al., 2019***). Mimicking experimental data (***Roopun et al., 2008***), the model produces γ rhythms in the superficial layers and beta 2 ($\sim$ 25Hz) in the deep layers in the presence of adequate stimulation (sensory *in vivo*, excitatory agonist *in vitro*) (***Kramer et al., 2008***). If the excitation is diminished *in vitro* (modeling the disappearance of the sensory signal), both deep and superficial layers switch to a β_1 ($\sim$ 15 Hz) rhythm

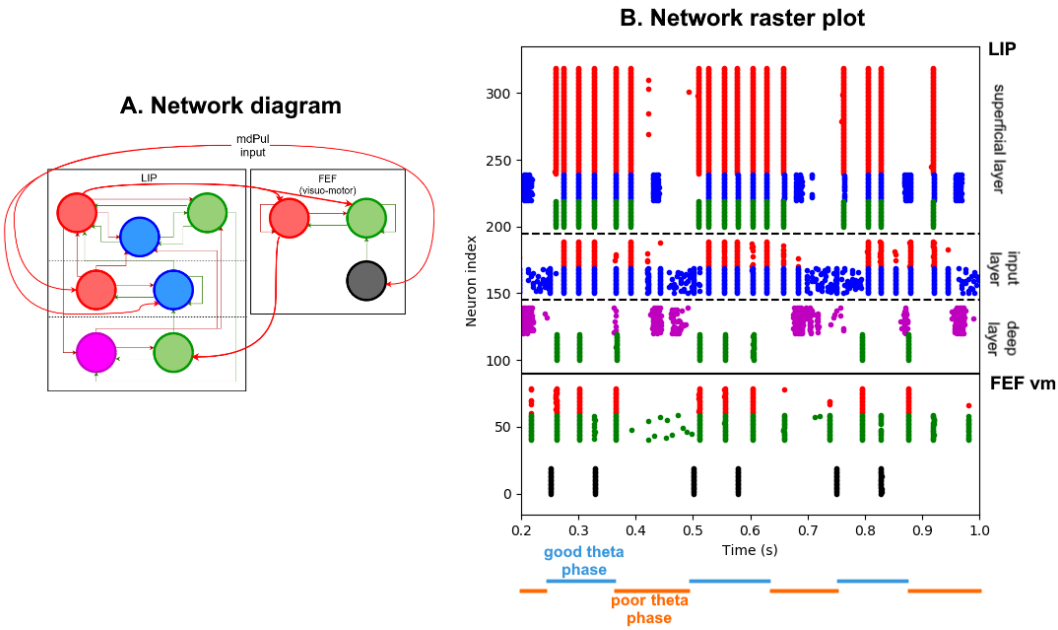

Figure 3. A. Diagram of the LIP and FEF visuo-motor module model (without decision cells). B. Interactions of the LIP and FEF visuo-motor network in a 1-second long simulation with an alternation of good and poor θ phases pulvinar inputs reproduces experimentally observed rhythms. The raster plot shows the activity of LIP on top, and that of FEF visuo-motor cells at the bottom. No target was presented. LIP produces an alternation of γ and β_1 rhythms, FEF visuo-motor cells produce β_2 oscillations only during the good θ phase.

(***Kramer et al., 2008***). A single period of the β_1 rhythm concatenates a single γ period and a single β_2 period (***Kramer et al., 2008***). Both the γ period and the β_2 period composing the β_1 are initiated by rebound from inhibition; this allows the β_1 to remain active even at low levels of excitatory input (***Kramer et al., 2008***). As a consequence of the unusual physiology producing it, this rhythm exhibits unique functional properties: a superficial γ-rhythmic cell assembly excited by an initial stimulus maintains persistent activity as part of a β_1 rhythm after the cessation of the initial stimulus; and multiple cell assemblies can be added and subtracted from this “working memory buffer" without interference (***Gelastopoulos et al., 2019***). Thus, this model is especially relevant to our task, which involves maintaining the cue location in working memory for up to 1.6s, until target appearance.

The second inspiration for the LIP module is a model of the effects of (attentional) cholinergic modulation on the potentiation of γ power in the superficial layers of sensory cortex (***Lee et al., 2013***). In the presence of cholinergic modulation, beta rhythms delivered to deep layers activate SOM interneurons, which in turn produce slowly decaying inhibition that suppresses granular layer FS cells. This results in disinhibition of granular layer RS cells, and leads to more γ power in both granular and superficial layers. In summary, the γ rhythm forms from the interaction of RS and FS cells in the input layer, dependent on the FS cells receiving slow inhibition from deep layer SOM interneurons.

As in the working memory model, the circuitry of our LIP module produces a β_1 “concatenation" rhythm in the absence of input from mdPul or FEF (i.e., in the poor θ phase, Figure 4-B). We interpret this β_1 as a “post-excitation" rhythm, since in our model it always occurs following excitation – both that of cue presentation and that of the (prior) good θ phase. As in the previous model of attention (***Lee et al., 2013***), beta input to deep SOM interneurons in our LIP module partially suppresses granular FS cells, leading to disinhibition of granular RS cells. (Granular FS cells remain active, but come under the control of granular RS cells.) When this disinhibition is combined with increased excitatory input to the granular layer, a γ rhythm results, which then propagates to the superficial layer (see Figure 3 and Figure 4-A). During the good θ phase, the LIP module receives exactly these two inputs – a β_2 input from FEF exciting deep SOM interneurons, and an α input from mdPul

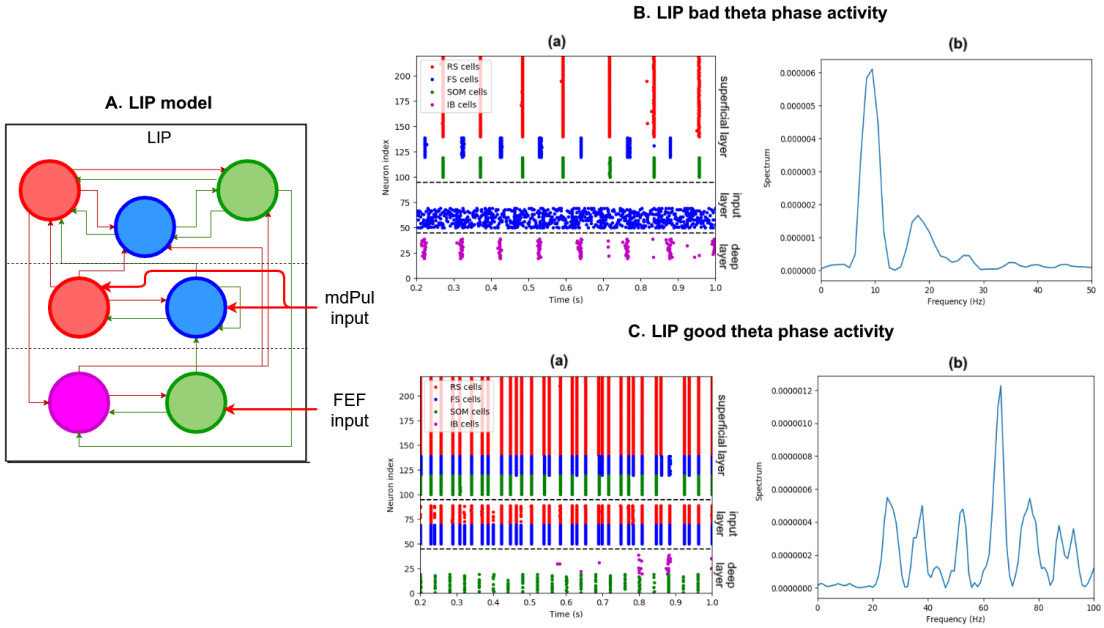

Figure 4. A. Diagram of the LIP model. Excitatory neurons and synapses are shown in red while inhibitory neurons and synapses are shown in green. **B. Reproduction of LIP β_1 oscillatory rhythm, characteristic of the poor θ phase.** (a) raster plot of a 1-second simulation of LIP activity with lack of inputs, corresponding to the poor θ phase, showing a β_1 oscillatory rhythm obtained through period concatenation. (b) power spectrum of the LFP generated by superficial RS cells for the same simulation, with a peak in the β_1 frequency band. **C. Reproduction of LIP γ oscillatory rhythm, characteristic of the good θ phase.** (a) raster plot of a 1-second simulation of LIP activity in the presence of inputs, corresponding to the good θ phase, showing a γ oscillatory rhythm obtained through the disinhibition of the granular layer. (b) power spectrum of the LFP generated by superficial RS cells for the same simulation, with a peak in the γ frequency band.

exciting the granular layer. Thus, as in the previous model (***Lee et al., 2013***), FEF beta input to the deep layers of LIP *creates* the potentiated γ in the superficial layers of LIP during the good θ phase.

The α rhythmic input that excites the RS and FS cells of the LIP module's granular layer differs from the tonic input used previously (***Lee et al., 2013***), but the result is the same (Figure 4-C). We model mdPul input excitation as a series of AMPA-like excitatory pulses arriving at α frequency. Since mdPul neurons are unlikely to fire in complete synchrony, the rise and decay time of the input synapses to LIP has been increased (from $t_{rise} = 0.1ms$ and $t_{decay} = 0.5ms$ in AMPA synapses within the network, to $t_{rise} = 2ms$ and $t_{decay} = 10ms$ in input synapses, see Figure S4-A). However, having input synapses with a shorter rise and decay time does not prevent the LIP module from generating a γ rhythm (Figure S4-B), though it reduces its frequency. The γ rhythm also persists when the rise and decay times of the input synapses are increased (Figure S4-C). (We explore the range of parameters for which this mechanism produces a superficial γ more fully in Section Robustness and flexibility of the LIP module.)

A model of FEF visuo-motor cells produces β_2 oscillations under pulvinar stimulation

Similar to the visual module, the FEF visuo-motor module consists of pyramidal regular spiking (RS) cells that are interconnected with slow interneurons (SOM cells), themselves inhibited by VIP cells (Figure 5-(a)). (The FEF visuo-motor module also includes decision cells which are only active when a target is present (Section Mechanisms of target detection), and thus do not play a role in model behavior during the cue-target delay.) RS and SOM cells receive excitatory inputs from LIP, and VIP cells receive excitatory inputs from mdPul. The LIP inputs arise from the LIP module in the fully connected model, and are synthetic inputs mimicking the LIP module's input otherwise. In line with experimental data (***Fiebelkorn et al., 2019***) (and the behavior of our LIP module), LIP inputs are at a γ frequency during the good θ phase and at a betal frequency during the poor θ phase, and mdPul inputs are at an α frequency, arriving only during the good θ phase.

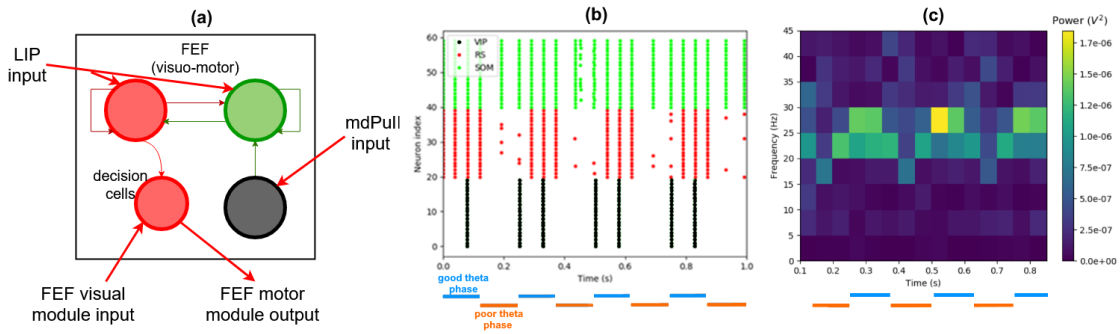

Figure 5. Reproduction of FEF visuo-motor cell rhythms. (a) Diagram of the FEF visuo-motor model. (b) Raster plot of a 1s-long simulation of FEF visuo-motor cells with alternating good and poor θ phases : VIP cells stimulated only during the good θ phase enable RS and SOM cells to form a β_2 rhythm through disinhibition. The activity of the decision cells is not shown on this raster plot. (c) Spectrogram of the LFP generated by visuo-motor RS cells in the same simulation, showing a peak in the β_2 frequency range only in the good θ phase.

During the poor θ phase, the excitation-inhibition (E-I) balance between SOM and RS cells is such that the SOM cells (activated by tonic excitation) silence the RS cells. VIP cells (which receive neither tonic excitation nor external input during this phase) are quiescent. During the good θ phase, VIP interneurons, stimulated by mdPul, fire following the input α rhythm, periodically inhibiting SOM cells. This alters the E-I balance between RS and SOM cells, allowing the RS cells to take control of SOM cell activity. The timescale of the inhibition generated by SOM cells determines the frequency of the rhythm resulting from RS-SOM cell interactions, a β_2. This module exhibits a motif similar to that which creates a γ in LIP: when the interneurons (SOM and PV, respectively) coupled to RS cells are too active, rhythms do not appear; when these interneurons are inhibited (by VIP and SOM interneurons, respectively), an altered E-I balance allows rhythms (driven by RS cell firing) to emerge.

Figure 5-(b) shows a raster plot of a one second-long simulation of the FEF visuo-motor cell module, with θ-rhythmic synthetic input from LIP and mdPul reproducing alternating good and poor θ phase activity. RS cells are mostly quiet during the poor θ phase, but fire and entrain SOM cells to a β_2 rhythm during the good θ phase. This β_2 rhythm is visible in the spectrogram of the simulated local field potential (sLFP) for this network (Figure 5-(c)). Note there is a small offset between the start of VIP cell activity and RS cell activity in the good θ phase. Section Robustness and flexibility of the FEF visuo-motor module explores the role of the inputs and of some parameters of the FEF visuo-motor module on the generated rhythms.

Mechanisms of target detection

VIP neurons detect small changes in visual input to FEF visual cell module

In FEF, the model has three submodules, playing different functional roles. In addition to the visuo-motor module described above, a visual and a motor module determine the model's response to target presentation. The appearance of a target on the screen is simulated as a transient excitatory input to FEF visual cells at a γ frequency (50Hz), presumably coming from visual area V4 (or other sources).The visual module consists of RS, FS, VIP and SOM cells (see diagram, Figure 3-A). We placed this target detection network in FEF visual cells to match current knowledge of the visual attention network, but we note that similar mechanisms could be instantiated in LIP.

The heart of the target detection circuit is the VIP–SOM interaction; both of these cells receive enhanced visual input (presumably from V4) upon target presentation. VIP and SOM cells are known to mutually inhibit each other (***Tremblay et al., 2016***), but while VIP have only local connections to SOM cells, SOM cells have global connections to VIP cells (***Karnani et al., 2016***; ***Zhang et al., 2014***). This is instantiated in the module by separating the cells into two clusters, each representing a different location in visual space. While SOM cells inhibit VIP cells from both clusters, VIP cells inhibit only SOM cells in the same cluster. RS and PV cells likewise connect only to other

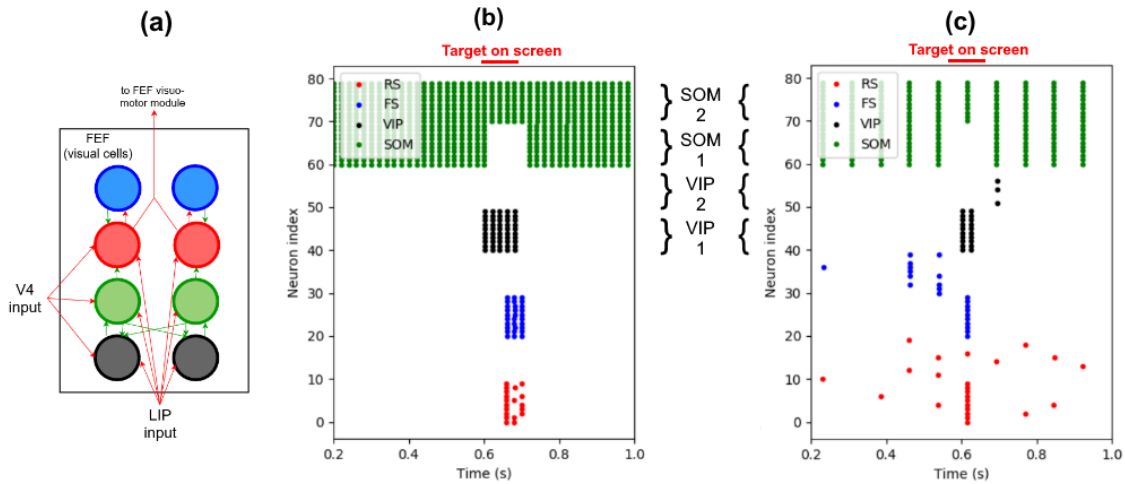

Figure 6. Oscillatory activity in FEF visual cells around target presentation. (a) Diagram of the FEF visual cells model (b) Raster plot of a 1-second simulation of FEF visual cells with inputs corresponding to the good θ phase, with a target appearing on screen at t=600ms for a duration of 100ms, leading to γ activity in RS cells. (c) Raster plot of a 1-second simulation of FEF visual cells with inputs corresponding to the poor θ phase, with a target appearing on screen at t=600ms for a duration of 100ms, leading to single spike activity in RS cells.

cells within the same cluster (Figure 6-a). The physiology of VIP interneurons – which exhibit large responses to relatively small inputs – also plays an important role in the model dynamics.

When no target is present on screen, all SOM, RS and VIP cells in the module receive input from LIP. The sizes of the inputs are such that SOM cells are active, and SOM inhibition silences VIP and RS cells. When a target appears, a smaller γ input (presumably coming from visual areas, possibly via LIP) further excites the SOM, RS and VIP cells of one cluster. Within this cluster, SOM cells, which were already highly active, do not change their spiking pattern. The VIP cells in this cluster therefore receive the same amount of inhibition, but a higher amount of excitation, which causes them to fire. VIP firing then temporarily silences SOM cells, disinhibiting RS cells and enabling them to fire. The interaction of RS and FS cells then produces a burst of γ rhythmic activity (Figure 6-b) in response to target appearance. Though such increased excitability of RS cells could be obtained though many different mechanisms, the VIP and SOM cell interaction amplifies a small difference in excitation between two visual regions, resulting in a large RS cell response to even a small increase in excitation. We believe these mechanisms play an important role in detecting near-threshold visual stimuli, such as the low contrast target of the task we are modeling. We discuss the robustness of this module in more detail in Section Modeling choices in the FEF visual module.

In this module, the influence of θ rhythm phase is via the input from LIP, which is a γ rhythm in the good θ phase and a β_1 rhythm in the poor θ phase. FEF visual RS cells spike at target presentation during both good and poor θ phases, producing either a γ burst or single spikes, respectively (Figure 6-c). Note that target detection in the FEF visual cell module is not yet adequate for a “hit" to be recorded for the model. This module’s response to a target appearing on the screen still needs to be transmitted to the FEF visuo-motor module, where a decision to act on it is made by what we call “decision cells". Only the spiking of decision cells following target appearance is considered a “hit". As will be shown in the next section, the activity of the visuo-motor module and decision cells are strongly affected by the θ rhythm.

FEF decision cells and motor cells model enable action following target detection

The output of FEF visual and visuo-motor cells is transmitted to a set of RS cells in FEF that we refer to as decision cells, whose spiking activity initiates action in response to target detection. These “decision cells" are modeled as simple RS pyramidal cells. Input from FEF visuo-motor cells sets

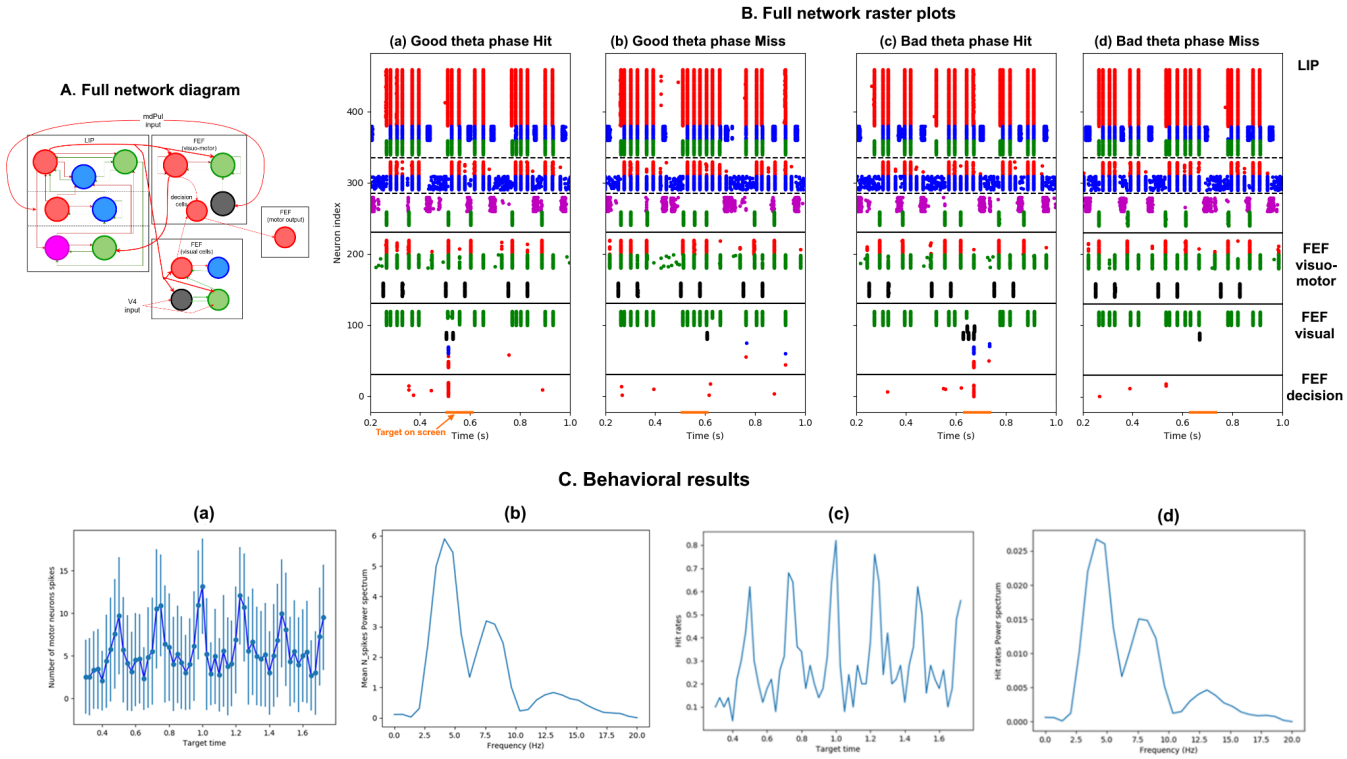

Figure 7. A. Diagram of the full LIP and FEF model. B. Raster plots of the LIP and FEF network in a 1-second long simulation with an alternation of good and poor θ phases pulvinar inputs, and target appearing in the good or poor θ phase. The raster plots shows the activity of LIP on top, that of FEF visuo-motor cells right below, that of FEF visual cells below them, and that of FEF decision cells at the bottom. A target was presented for 100ms in the good θ phase in (a) and (b), with only (a) leading to significant decision cells activity. A target was presented for 100ms in the poor θ phase in (c) and (d), with only (c) leading to significant decision cells activity. **C. Network decision cells response to target appearance and hit rates varies with a θ frequency.** (a) Number of decision cells spikes (with mean and standard deviation) following target appearance as function of the time of target appearance. (b) Power spectrum of the number of decision cells spikes, showing a peak at a low θ frequency (4Hz). (c) Hit rates following target appearance as function of the time of target appearance. (d) Power spectrum of the hit rates, showing a peak at a low θ frequency (4Hz).

the threshold of decision cell spiking, determining how likely they are to respond to (simultaneous) input from visual cells when a target appears (Figure 6 (a) and (c)). Decision cells then send the information to act on the target to motor cells. There is evidence to suggest that FEF motor neurons participate in overt and covert visual responses to the target, so we have modeled FEF motor neurons as RS cells initiating the target response. FEF motor cells can receive inputs from different brain areas that are not modeled here, to have an appropriate response depending on the task (for example initiate eye movement).

Task performance

Network response to target appearance is greater during the good θ phase

To test whether the network dynamics observed during good and poor θ phase also affect target detection, we varied the time of appearance of a simulated target (a 100ms-long train of γ frequency excitatory pulses to FEF visual neurons) across several θ cycles. The model's response to the target depended on its timing relative to the ongoing θ cycle (Figure 7). More precisely, the number of FEF decision cells spikes following target appearance was higher when the target appeared in the good θ phase (or at the transition from poor to good θ phase) compared to when it appeared in the poor θ phase (or at the transition from good to poor θ phase; Figures 7-B., 7-C. (a) and (b)). (Note that the timing of target appearance refers to the onset of the target input.)

We translated FEF decision cell spiking into a hit rate via thresholding: we considered that a trial was a "hit" if more than half the FEF decision cells neuron population spiked at least once during

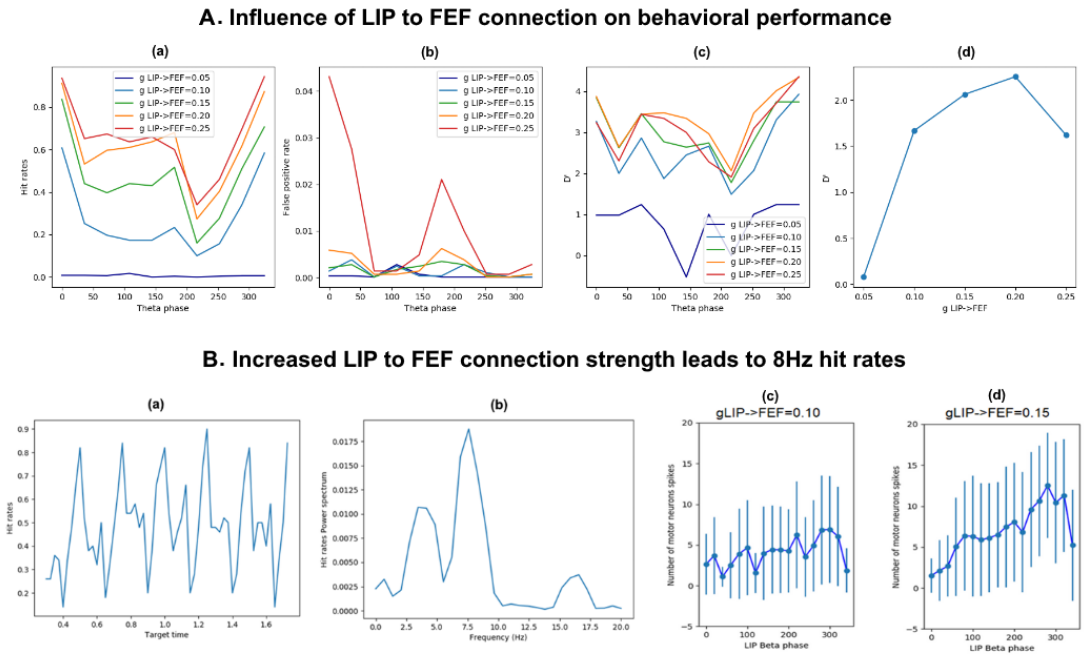

Figure 8. A. The strength of the LIP→FEF visual module connections increases hit rates and false alarm rates, with intermediary values leading to higher D' sensitivity index. (a) hit rates as function of the θ phase, with different values of the LIP→FEF visual module connection strength. (b) false alarm rate as function of the θ phase, with different values of the LIP→FEF visual module connection strength. (c) D' measure as function of the θ phase, with different values of the LIP→FEF visual module connection strength. (d) D' measure over the whole theta cycle as a function of the LIP→FEF visual module connection strength. **B. Increased LIP→FEF visual module connection strength leads to a stronger 8Hz component in the hit rates.** (a) hit rates following target appearance as function of the time of target appearance, with conductance of LIP→FEF visual module synapses of 0.15. (b) power spectrum of the hit rates, showing a peak at a high θ frequency (8Hz). (c) Number of decision cells spikes in the poor θ phase as function of LIP β_1 oscillation phase, with low LIP→FEF visual module connection strength. (d) Number of decision cells spikes in the poor θ phase as function of LIP β_1 oscillation phase, with high LIP→FEF visual module connection strength.

the 100ms-long window where the target was presented. In agreement with behavioral data, hit rates vary depending on the time of target appearance, and follow a 4 Hz θ rhythm (Figure 7-C. (c) and (d)).

Both hit rates and false alarm rates increase with the conductance of LIP to FEF visual cell synapses

The strength of the synaptic connections from LIP→FEF visual neurons have a large influence on hit rates (Figure 8). Increasing the strength of this connection increases hit rates in both good and poor θ phases. However it also comes with an increased false alarm rate, i.e., a higher probability of having more than half of the decision cells firing in any 25ms-long window outside target presentation (Figure 8-A). Computing the D' sensitivity index of the model reveals that intermediate values of LIP→FEF connectivity strength result in optimal task performance (that is, high hit rates and low false alarm rates).

Intermediate values of the conductance of LIP→FEF connections also give rise to a temporal profile of hit rates with a dominant 8 Hz (rather than 4 Hz) component. In these cases, in addition to a peak in hit rate at the beginning of the good θ phase (at 0 degrees), there is a second, smaller peak in hit rate at the beginning of the poor θ phase (Figure 8-B, (a) and (b)). This is a result of LIP superficial RS spikes participating in β_1 oscillations, which excite FEF visual neurons, and rescuing target detection in the poor θ phase. Plotting the number of decision cells spikes following target appearance in the poor θ phase as a function of the phase of the LIP β_1 oscillation (Figure 8-B, (c) and (d)) reveals a strong influence of LIP beta phase on decision cells spiking for a medium (subplot (d)) but not for a low (subplot (c)) value of the LIP→FEF synaptic conductance (correlation coefficient 0.33, $p < 10^{-20}$, for medium $g_{\text{LIP}\rightarrow\text{FEF}}$).

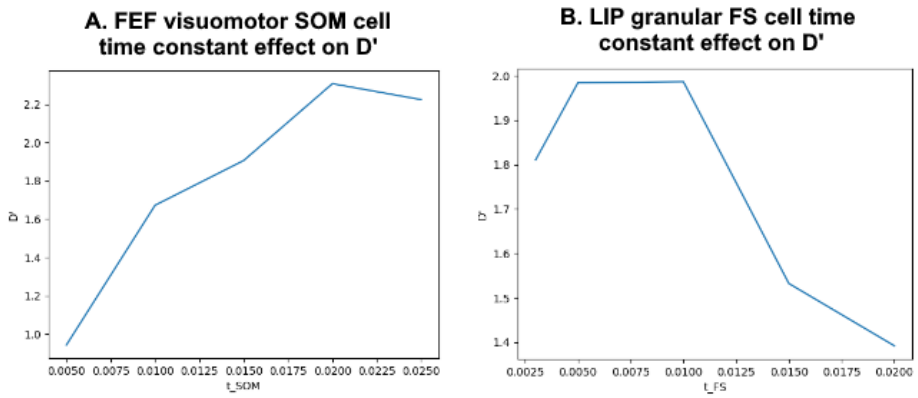

Figure 9. Changing FEF and LIP oscillatory frequency negatively impacts task performance. A. D' measure as a function of the FEF SOM cells inhibition time constant. B. D' measure as a function of the LIP FS cells inhibition time constant.

In behavioral data (***Fiebelkorn et al., 2013***), an 8 Hz rhythm in hit rate was observed for trials in which the target appeared within the same object as the cue, while a 4 Hz rhythm in hit rate was observed for trials in which the target appeared within a different object from the cue. Our model thus suggests that the deployment of attention towards a cued object induces a change in functional connectivity, moderately increasing the strength of LIP→FEF connectivity, with a resulting increase in performance (as reflected by an increase in D').

Target detection is optimized by FEF oscillations at beta frequency and LIP oscillations at γ frequency

One question that naturally arises from the previous results is whether the frequency of LIP and FEF rhythms is significant for task performance. To answer it, we modified the synaptic time constants of inhibition in LIP granular FS cells and FEF visuo-motor SOM cells, to vary their oscillatory frequency across the beta and γ ranges, and analyzed the temporal profile of hit rates in response to targets appearing at different times following cue presentation, as in the previous section.

Interestingly, similar effects on performance result from changing the frequency of LIP oscillations from γ to β_2 (Figure 9-A and S1-A) and from changing the frequency of FEF oscillations from β_2 to γ (Figure 9-B and S1-B). Either manipulation decreases hit rates for targets appearing at zero θ phase, while increasing the hit rates for target appearing throughout the poor θ phase. But though the mean hit rate over the whole θ cycle is not significantly decreased (and is even increased in the case of varying LIP granular FS inhibition), false alarm rates are greatly increased when the rhythms are altered, leading to a lower D' sensitivity index (Figure 9-A. and 9-B.). γ oscillations in LIP and β_2 oscillations in FEF therefore appear to be optimal for performance in this attention task, independent of the strength of the LIP→FEF connection. Further inspection reveals the mechanisms behind this frequency-dependence.

Effects of decreased inhibitory time constant of FEF visuo-motor SOM cells: Decreasing FEF SOM cells' inhibitory time constant increases the activity of FEF visuo-motor RS cells during both good and poor θ phase, which leads to an increased spiking of FEF decision cells even in the absence of a target on the screen. This spiking in the poor θ phase is not quite enough to elicit a false alarm on its own, which is why increased false alarm rates are only seen in the good θ phase (Figure S2-A). The effect of increased FEF visuo-motor RS activity on hit rates in slightly more complex. As these cells project to LIP deep interneurons, which inhibit granular layer FS cells, an increase in their activity biases the E-I balance in LIP granular layer towards less inhibition. In the poor θ phase, where inhibition is otherwise much stronger than excitation, this leads to an increased firing of granular and superficial LIP RS cells (and the appearance of γ oscillations); in the good θ phase, where excitation and inhibition are otherwise relatively balanced, the firing of LIP RS cells is slightly

decreased. This in turn leads FEF visual cells to fire more in the poor θ phase and less in the good θ phase (Figure S2-B), and therefore to increased hit rates in the poor θ phase and slightly decreased hit rates in the good θ phase.

Effects of increased inhibitory time constant of LIP granular FS cells: Increasing the time constant of FS cell inhibition in the granular layer of LIP leads to a slowing of granular and superficial LIP rhythms to beta frequencies, in contrast to the effects of changing the frequency of FEF visuo-motor cell rhythms, which mostly changed the θ phase of LIP superficial and granular layer oscillations, but not their frequency (see Figure S3). LIP projects to FEF visual neurons, pacing the activity of FEF visual SOM cells in particular, whose role is to prevent visual RS cells from spiking via inhibition that also exhibits a beta time scale. When LIP input rhythms are at beta or slower time scales, the pace of FEF visual SOM spikes allows windows of sufficiently low inhibition that FEF visual RS neurons are able to spike even in the absence of a target (Figure S2-C). This spiking translates into increased false alarm rates, as well as increased hit rates (though some of the hits are simply a consequence of intrinsic network activity, and not a response to target appearance).

Model robustness and flexibility

As shown in the previous sections, our model is able to reproduce both the neural dynamics and the behavioral results observed during rhythmic sampling in spatial attention(***Fiebelkorn et al., 2019***). In order to be relevant to the brain, our model must be somewhat robust to parameter changes. However, since LIP and FEF are involved in cognitive tasks other than rhythmic attention, it should also be flexible enough to allow different rhythms to appear as conditions are varied. This section will address both these issues by looking at the conditions under which oscillations arise in the different submodules of our model.

Robustness and flexibility of the LIP module

The activity of the LIP module depends on the rhythmic input it receives from FEF and mdPul, as well as on the tonic excitation given to its input layer. While α input from mdPul helps sustain γ oscillations, it does not play as important a role as the disinhibition mediated by the (top-down) beta from FEF (see Figure 10). The absence of mdPul α input to the LIP input layer reduces the frequency of superficial and granular layer oscillations, down to a low γ ($\sim 30Hz$, Figure 10-B). In this situation, the RS cells in the input layer spike mostly when they are disinhibited by the β_2 drive to LIP deep layer SOM cells, but can fail to fully take control of input layer FS cells in between deep SOM cell spikes. On the other hand, the absence of a β_2 input to the deep layer fully stops the activity of input layer RS cells and leads to LIP β_1 rhythmicity, just as in the poor θ phase (Figure 10-C). LIP good and poor θ phase rhythms also depend on the level of tonic excitation of input layer RS and FS cells (see Figure S6, and Influence of Tonic Excitation on LIP Behavior for ranges and model behavior outside of them).

It is noteworthy that though the LIP model is robust to some changes to the tonic excitation level, it is also able to produce different types of activity that could be needed in other cognitive tasks. For example, LIP's ability to direct attention to a highly salient stimulus in a bottom-up fashion (***Bisley et al., 2011***; ***Buschman and Miller, 2007***; ***Miller and Buschman, 2013***) can be reproduced in our model by giving a strong stimulation to its input layer (presumably coming from V4), which will start a γ rhythm even in the absence of mdPul and FEF input, as shown on Figure S6-B (see Discussion section for more details).

Robustness and flexibility of the FEF visuo-motor module

Similarly to LIP, the activity of the FEF visuo-motor module depends on the rhythmic input it receives from LIP and mdPul, as well as on the tonic excitation given to its RS and SOM cells. Pulvinar input – which enables VIP cell firing and leads to RS cell disinhibition – is required for the network to achieve a β_2 rhythm during the good θ phase: without mdPul input, RS cells are quiescent in both the good and poor θ phases (Figure S7-A). The frequency of mdPul input also plays a role

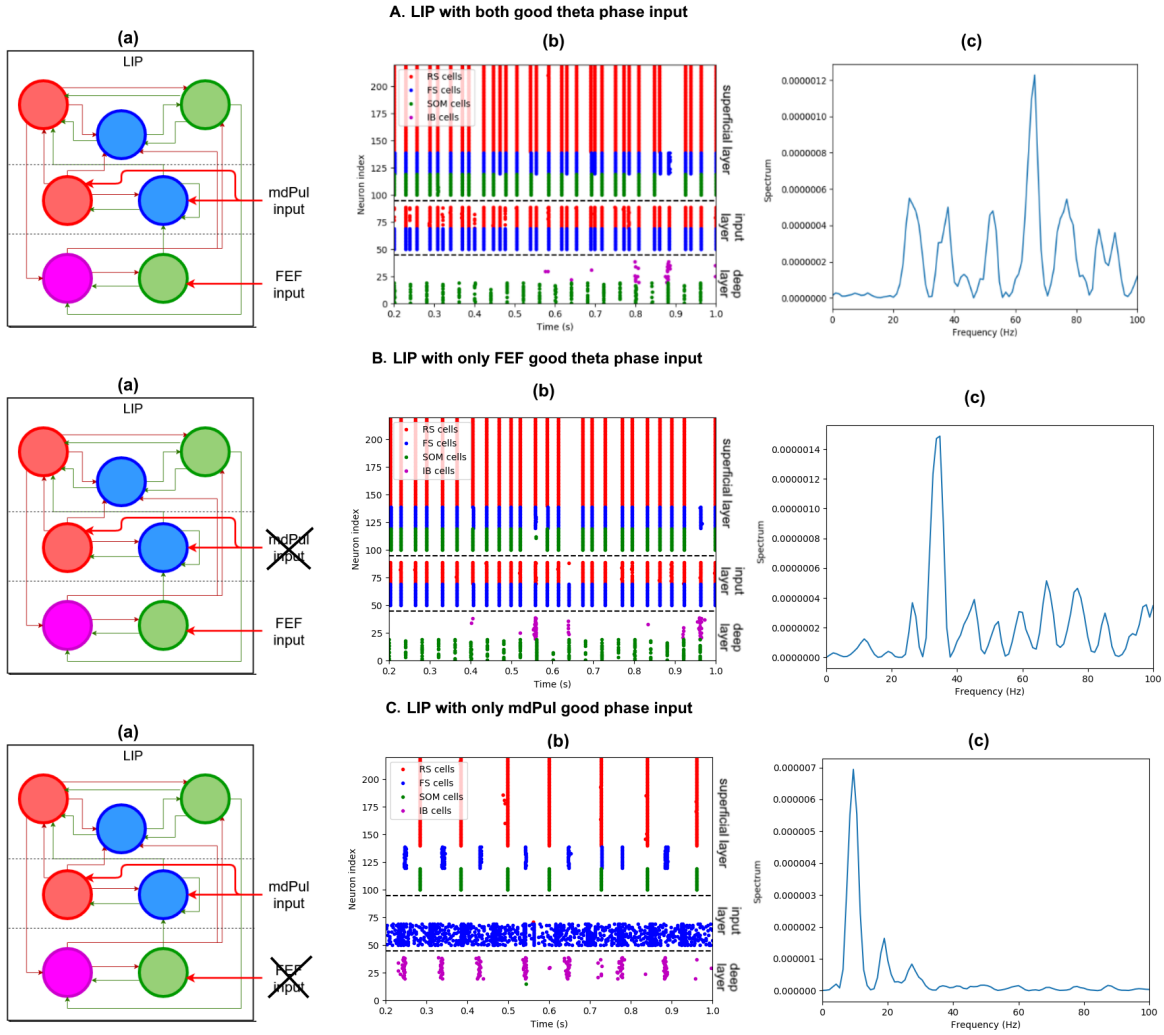

Figure 10. LIP good θ phase behavior depends on mdPul and FEF inputs A. LIP good θ phase behavior with both mdPul and FEF inputs ((a): diagram of the model, (b): Raster plot of a 1s-long simulation, (c) : power spectrum of the LFP generated by the network in this 1s-long simulation). B. LIP good θ phase behavior with FEF input but no mdPul input ((a): diagram of the model, (b): Raster plot of a 1s-long simulation, (c) : power spectrum of the LFP generated by the network in this 1s-long simulation). C. LIP good θ phase behavior with mdPul input but no FEF input ((a): diagram of the model, (b): Raster plot of a 1s-long simulation, (c) : power spectrum of the LFP generated by the network in this 1s-long simulation).

in generating sustained β_2 oscillations: input at θ or slower frequencies does not provide enough disinhibition to RS cells for them to take control of SOM cells during the entire good θ phase (Figure S7-B). However, model behavior is preserved when mdPul input arrives at frequencies faster than α, and when the width of mdPul excitatory pulses is varied (Figure S7-C). The frequency of the alternation of the good and poor θ phases needs to be below half of mdPul α frequency for the network to achieve a β_2 rhythm in the good θ phase (Figure S7-D).

LIP input to RS and SOM cells also influences the activity of the FEF visuo-motor module. Simply removing this input causes RS cells to fire at a β_1 instead of β_2 rhythm during the good θ phase, since they do not receive enough excitation to fire outside the windows of disinhibition provided by VIP spikes (Figure S5-A). For the same reason, LIP input at a frequency in the α range or lower leads to LIP exhibiting a β_1 rhythm in the good θ phase (Figure S5-B). LIP input at a β_1, β_2, or γ frequency are needed to achieve the desired β_2 frequency in LIP RS cells. In particular, this means that the FEF visuo-motor β_2 characteristic of the good θ phase can occur even if LIP is still producing the β_1 characteristic of its poor θ phase dynamics. Therefore, our model suggests that the transition from the poor to the good θ phase is likely being initiated by FEF, which then recruits LIP in a top-down fashion. Increasing the frequency of LIP input above the γ range causes FEF visuo-motor RS cells to fire at a frequency faster than β_2, provided that the input is strong enough.

Even at experimentally observed frequencies, the strength of LIP input influences FEF visuo-motor rhythms (Figure S5-C). A too-weak input does not provide enough excitation for FEF to produce a β_2 rhythm during the good θ phase (it produces a β_1 rhythm instead), while with a too-strong input FEF RS cell spiking follows the LIP input rhythm (at a β_1 frequency during the poor θ phase, and a γ frequency in the good θ phase). Importantly, though this behavior is undesirable for the rhythmic attention task we are modeling here, the activation of the FEF visuo-motor module by LIP input in the absence of mdPul stimulation may represent a bottom-up attentional state, in which the network responds to the appearance of a highly salient target in a bottom-up fashion.

Finally, just as LIP activity depends on the tonic excitation given to its input layer RS and FS cells, FEF visuo-motor activity depends on the tonic excitation given to its RS and SOM cells (S8).

Modeling choices in the FEF visual module

While simpler versions of the FEF visual module are still able to detect changes in contrast, they exhibit some disadvantages that motivated our modeling choices (Figure 11). A model including only RS and FS cells (Figure 11-A) is able to exhibit a γ burst during target presentation in response to increased excitation of RS cells during target presentation (even without the disinhibition provided by VIP cells), provided that this excitation is strong enough. However, since RS cells have a larger capacitance than VIP cells, the strength of the target input must be at least 1.5 times larger than the background stimulation from LIP to result in γ rhythmicity (Figure 11-A b and c), which we interpret as detection of a high contrast target. Thus, the VIP and SOM cell circuit in the visual module plays an important role in the detection of near-threshold contrast changes, and, presumably, other near-threshold stimuli.

In contrast, simulations of a model including only one interconnected network of RS, FS, VIP, and SOM cells (as opposed to two clusters of cells with different inter- and intra-cluster connectivity) were unable in our hands to satisfactorily exhibit robust target detection (Figure 11-B). Robust target detection in this circuit depends on VIP cells being silenced by SOM cells when no target is present, and SOM cells being silenced by VIP cells during target presentation, during both the good and the poor θ phase (that is, with a background input from LIP in the γ or β_1 range). We were unable to achieve this behavior for any of the conductances of VIP→SOM inhibitory synapses or levels of tonic excitation to VIP and SOM cells tested. An example of an unwanted behavior in a model without clusters is shown in Figure 11-B (subplot (b) and (c)), where the inhibition from SOM to VIP is strong enough to ensure VIP cells don't spike outside target presentation in the good θ phase (that is, when LIP input is in the γ range and SOM cells are also active at a γ rhythm), but not in the poor θ phase (when LIP input and SOM cell spiking are at β_1 frequency). Increasing

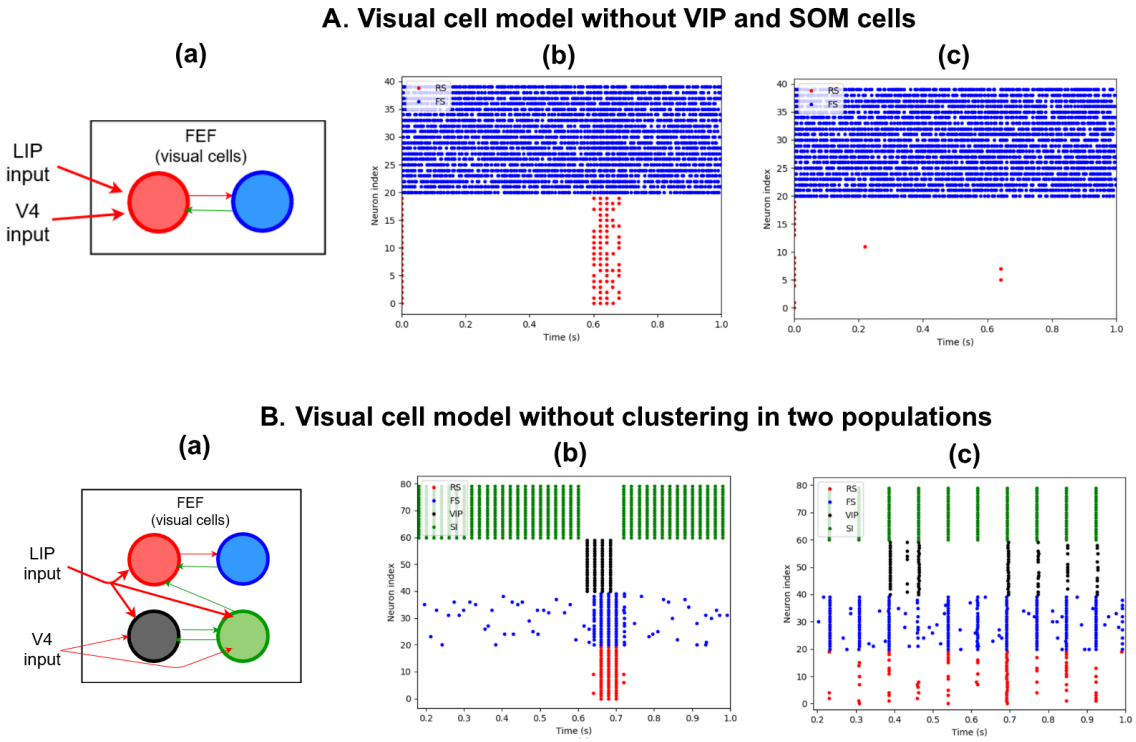

Figure 11. A. A model without VIP and SOM cells fails to detect a small change in input (a) Diagram of a FEF visual cells model without VIP and SOM cells (b) Raster plot of a 1-second simulation of the model, with a target input of strength 1.5 times the strength of the background input applied between 600ms and 700ms, leading to γ activity in RS cells. (c) Raster plot of a 1-second simulation of the model, with a target input of strength 0.5 times the strength of the background input applied between 600ms and 700ms, leading to no activity in RS cells. **B. A model without clustering into two cell population leads to false detection in the poor θ phase** (a) Diagram of a FEF visual cells model without clustering into two populations (b) Raster plot of a 1-second simulation of the model in the good θ phase, with a target input applied between 600ms and 700ms, leading to γ activity in RS cells only during target presentation. (c) Raster plot of a 1-second simulation of the model in the poor θ phase, with a target input applied between 600ms and 700ms, leading to RS cells activity outside of target presentation.

the inhibition from VIP to SOM leads to an inability of VIP cells to spike at target presentation. Separating SOM and VIP cells into two clusters enables a finer tuning of the inhibition between them (for example, instead of receiving an all-or-nothing inhibition from SOM cells, VIP cells can receive inhibition from half of the SOM cells), which helps achieve the model behavior necessary for task performance under a variety of different constraints.

Discussion

We propose a biologically detailed model of LIP and FEF circuits, capable of reproducing the complex oscillatory dynamics observed in these regions during spatial attention (***Fiebelkorn et al., 2019***) in response to rhythmic pulvinar input, the presence and absence of which defined the good and poor θ phases observed experimentally during task execution (***Fiebelkorn et al., 2013***, ***2019***). The model is composed of different modules: an LIP module with a laminar structure capable of producing β_1 and γ oscillations, and motivated by previous work on memory and attention (***Kramer et al., 2008***; ***Lee et al., 2013***); and an FEF module including visual, motor, and visuomotor functional submodules, capable of producing β_2 oscillations and detecting the appearance of a target on a screen.

In this model, biophysically detailed rhythmic dynamics interact to support enhanced sensitivity in visual target detection during the good θ phase, while maintaining functional flexibility – for example, the potential of target detection during the bad θ phase. The incorporation of mechanisms originally developed to illuminate brain function in related but distinct cognitive contexts is a further constraint on the realism and flexibility of our model.

Our work shows that the strength of the conductance of LIP→FEF synapses can control the experimentally observed shift in hit rate periodicity from 4 Hz (for the uncued object) to 8 Hz (for the cued object). It suggests that while pulvinar primes LIP and activates FEF, it is FEF that elicits γ-rhythmic output from LIP in the context of top-down attentional control. It shows that the frequency of observed rhythms optimizes these interactions and the sensitivity of target detection, suggesting that these rhythms, rather than being epiphenomena, are key to the function of attention in the brain. Finally, our model suggests hypotheses about how multiscale rhythmic coordination may serve to sequence and segregate the activities of perceptual and motor systems.

LIP to FEF Connectivity Controls the Frequency of Perceptual Sensitivity

Our model replicates experimental results at the behavioral level, with hit rates that vary with the θ phase of pulvinar input to the cortex and which are increased during the good θ phase (i.e. during pulvinar stimulation). In the FEF visual module, VIP cells enable the detection of low-contrast targets. Our work suggests that increasing the conductance of LIP→FEF synapses onto FEF visual cells increases first hit rates and then false alarm rates, so that intermediate values of connection strength lead to optimally sensitive target detection. These intermediate values of LIP→FEF visual module connectivity are also associated with a strong 8Hz θ component in the hit rates, which has been associated with attention towards a cued object in (***Fiebelkorn et al., 2013***).

We suggest that the appearance of a cue on the screen could enhance the connection from LIP→FEF visual module, leading to increased perceptual sensitivity especially during the poor θ phase and an 8 Hz dominant frequency in the hit rate spectrum. In other words, the 8 Hz hit rates in our model do not come from the division of a 4 Hz rhythm into multiple possible target locations, as previously suggested for similar data (***Landau and Fries, 2012***), but are a consequence of the increased LIP→FEF connection strength for the cued object. Our study also shows that an excessively strong LIP→FEF conductance leads to high false alarm rates, which may be connected to pathophysiological consequences such as hallucinations, as FEF visual cells detect a target even when nothing is present on the screen.

Interacting Rhythms in FEF and LIP Mediate the Competition Between Top-Down and Bottom-Up Control of Visual Attention

We observed that the rhythms in our network do not operate independently, but interact with one another to give rise to the observed neural activity and behavior. FEF visuomotor β_2 rhythm is essential to give rise to LIP γ, at least in the context of our task where LIP input layer does not receive a strong stimulation. In the model, the disinhibition of FEF visuomotor cells by pulvinar inputs activates a β_2 oscillation in the good θ phase. In turn, this FEF β_2 elicits γ oscillations from LIP, by effectively disinhibiting LIP granular layer pyramidal cells. LIP γ oscillations act to enhance sensory processing in the network by stimulating FEF visual cells, making them more likely to detect a target. FEF visuomotor β_2 oscillations in the good θ phase have two effects, both of which lead to increased hit rates: first they induce the previously described LIP γ oscillations, and second they directly excite decision cells. Thus, we think of the FEF visuomotor module as *leading* the rhythmic attention process in a top-down manner, and our model makes the prediction that the good θ phase is associated with the appearance of β_2 oscillations in FEF *before* γ oscillations in LIP.

Under different stimulation parameters, our model is also able to generate LIP γ oscillations without FEF β_2 input, provided that the tonic excitation given to LIP granular layers is strong enough. In particular, this means that a very salient stimulus, by providing strong excitation to the LIP input layers, could lead to enhanced sensory processing in a bottom-up fashion. FEF visuomotor cells are able to produce a β_1, a β_2 or a γ depending on the strength of inputs from LIP; thus, FEF could participate in different (rhythmically-connected) functional networks depending on whether visuomotor circuits are activated by highly salient as opposed to near-threshold stimuli.

An important recent computational model (***Jaramillo et al., 2019***) suggests that pulvinar functions by modulating the gain of feedforward (FF) cortico-cortical connectivity, and by altering the

balance between feedforward and feedback (FB) cortico-thalamo-cortical (CTC) pathways. This work draws on the fact that the pulvinar interacts with the cortex via two pathways: in addition to feedback pathways in which projections return to the deep layers of the cortical area from which its input arrives, pulvinar participates in feedforward pathways in which cortical input originating in one area (A) activates projections to the granular layers of a different cortical area (B), "boosting" the direct connections from area A to area B. In this previous model, it is the latter cortico-thalamo-cortical (CTC) feedforward pathway through which pulvinar excitability (which is fixed for the duration of a trial) changes the strength of cortico-cortical connectivity (***Jaramillo et al., 2019***). In our model, the gain of feedforward connectivity (as indexed by the conductance of synapses from LIP→FEF) plays a similar role in optimizing the network's sensitivity for target detection, representing the difference between cued and uncued locations. Our work provides a novel explanation, however, of the mechanisms by which increasing LIP→FEF connectivity leads to a doubling of the frequency of fluctuations in hit rate.

This prior work also addressed how pulvinar activity could alter rhythmicity in cortex. In this work, V4 rhythms at lamina-specific frequencies were modeled via E-I networks with lamina-dependent timescales of inhibition, giving rise to a superficial γ and a deep α. Feedback connections arising from the thalamus target interneurons in deep layers ((***Cruikshank et al., 2010***); (***Zhou et al., 2018***)., 2018; (***Audette et al., 2018***)). Thus, in this previous work, pulvinar feedback pathways inhibit deep layer excitatory cells, resulting in less α; and the disinhibition of deep layer E-I networks explains experimental observations that pulvinar lesion results in an increase in α rhythmicity in V4 ((***Zhou et al., 2016***)). In contrast, in our model, it is top-down β from FEF that disrupts LIP α, even though pulvinar input to LIP granular layers also contributes to the disruption of LIP's concatenation β_1 rhythm. Our model suggests that pulvinar lesion might indirectly increase low-frequency (β_1) power in LIP, just as it increases α power in V4, although through a different mechanism.

Our model also highlights other mechanisms by which network sensitivity is optimized. These mechanisms, though also mediated by the pulvinar, are distinct from both the FF CTC pathway and the competition between FF and FB CTC pathways explored in prior work (***Jaramillo et al., 2019***). Due to the way pulvinar inputs are simulated, our model supports an interpretation whereby LIP is the target of a FF CTC pathway originating in a lower-level visual area, such as V4, while FEF is the target of a FB CTC pathway. The influences of pulvinar on LIP and FEF are thus distinct anatomically and dynamically: pulvinar input helps to create a β_2 rhythm in FEF and a γ rhythm in LIP during the good θ phase. We suggest that these dynamic changes, rather than biasing a competition between FF and FB information transmission, allow the pulvinar to increase the precision of both FF and FB information transmission, effectively optimizing the sensitivity of the network to target appearance during the good θ phase. This increase in the precision of information transmission is due to the deployment of different rhythmic dynamics in the good and poor θ phases: in the good θ phase, an FEF β_2 mediates top-down information transmission as well as changing the temporal dynamics and lowering the threshold for target detection, while an LIP γ mediates bottom-up information transmission; in the poor θ phase, information transmission between FEF and LIP (i.e., spiking in FEF deep layers and LIP superficial layers) occur at alpha frequency (which also changes the temporal dynamics and the threshold for target detection in FEF). Altering the frequencies of either the FEF β_2 or the LIP γ decreases the sensitivity of the network.

Timescales of Observed Rhythms Optimize Task Performance

The frequency of FEF and LIP oscillations in our model has consequences for task performance, and the values typically reported in experiments are in fact optimal to achieve high sensitivity in our attention network. More precisely, increasing the oscillatory frequency of FEF visuomotor cells from β_2 to γ or reducing LIP oscillatory frequency during the good θ phase from γ to β_2, by changing the time constants of local inhibition, leads to higher false alarm rates, with little to no benefit on hit rates.

The optimization of network sensitivity by FEF β_2 and LIP γ results from the way that these

rhythms and their interactions subtly and differentially alter the excitation/inhibition balance in different layers and populations of LIP and FEF during different phases of the θ rhythm (see Results). These observations point to one important role of rhythms in mediating the effects of attention. However, an account of the effects of rhythms in terms of the E/I balance of FEF and LIP neuronal populations is incomplete, as it omits the temporal dynamics of both neural activity and its behavioral consequences. In both experimental data (***Fiebelkorn et al., 2013***, ***2019***) and our model, hit rate (and false alarm rate) vary not only between "conditions" (i.e., cued vs. uncued object/LIP→FEF connectivity, time scale of inhibition/rhythmic frequency), but also in time. The phase of θ, FEF β_2, LIP γ, and pulvinar α all have an effect on target detection (and its sensitivity).

We suggest that these temporal dynamics of network activity are not coincidental or epiphenomenological, but play important functional roles. The first of these is to synchronize and sequence precise monitoring and information transmission with (multiple) other computational processes occurring in other brain regions, each of which may have a different characteristic frequency (for example, β_2 for motor processes, and γ for visual processes). The second is to provide periodic windows of enhanced sensitivity, that enable precise monitoring of a given region of the visual field with acceptable temporal "coverage", while also minimizing energetic cost and allowing monitoring to be interleaved with other computational imperatives, including monitoring of other regions and motor planning and execution. We further elaborate on this sequencing and segregation of cognitive functions below.

Rhythmic Sampling and Turn-Taking Between Sensory, Cognitive, and Motor Networks

As the good θ phase is associated with improved sensory perception and behavioral performance in attention tasks (***Fiebelkorn and Kastner, 2019b***), one could wonder what need is served by the poor θ phase – and, indeed, the θ rhythm itself – in the first place.

One possibility is that the θ rhythm is a solution to the necessity of attending to multiple objects "at once", allowing the focus of attention to switch between objects θ-rhythmically. In this picture, the poor θ phase for the representation of one object or location would occur simultaneously with the good θ phase for the representation of another object or location (***Fiebelkorn et al., 2013***; ***Landau and Fries, 2012***). In our model, this could be achieved with multiple copies of LIP and FEF representing one cortical column for each object to be monitored; pulvinar inputs would select the attended object at any point in time, and manage switching the attentional focus. Even when attention is deployed at a single location, the break in attentional focus allowed by the poor θ phase would allow changes in one's surroundings and new salient stimuli to capture attention, and adapt behavior quickly, if needed. In this framework, the good θ phase could be described as a sampling phase for one location, while the poor θ phase could be described as an exploration phase (***Fiebelkorn and Kastner, 2019b***).

Finally, it has been hypothesized that the poor θ phase could enable the planning and execution of motor actions (***Fiebelkorn and Kastner, 2019b***). This hypothesis is consistent with the fact that β oscillations, which are characteristic of FEF activity in the good θ phase (***Fiebelkorn et al., 2018***), have been shown to act as a "hold" signal for motor areas (***Gregoriou et al., 2012***; ***Pogosyan et al., 2009***; ***Zhang et al., 2008***), effectively preventing movement. In this framework, the good and poor θ phase could be seen as enhancing sensory perception and motor execution, respectively. The task modeled here requires gaze fixation at the center of a screen, and the motor output consists in the release of a lever. Therefore, during this task our network participates in the deployment of attention and target detection, but not movement initiation. Target detection must be communicated to downstream motor areas to complete the task. Our results can be extended to account for motor actions by considering the impact of FEF decision and visuomotor cell activity on basal ganglia or superior colliculus, with visuomotor and decision cells mediating effective inhibition and excitation, respectively. Upon target detection, FEF decision cells would excite these downstream regions; but during the good θ phase, FEF visuomotor β_2 activity would prevent movement initia-

tion. (This effective inhibition by β_2 rhythmicity may not require synaptic inhibition, if β_2 functions as a “hold" signal.) Thus, we predict faster reaction times for hits during the poor θ phase than for hits during the good θ phase.

These different views on the role of the θ rhythm in perceptual sensitivity are not incompatible: the θ rhythm may be a mechanism that *interleaves* periodic attention to multiple objects or locations with motor execution, with movements occurring at the transitions between good and poor θ phases, each of which represents attention to one of several stimuli. Essentially, movement would be one more attentional focus, sequenced in turn with multiple salient regions of the visual field.

Methods

Equations governing model neurons

The model presented in this article consists of single-compartment Hodgkin-Huxley neurons adapted from ***Kramer et al.*** (***2008***) and ***Gelastopoulos et al.*** (***2019***), with the exception of LIP intrinsically bursting (IB) cells which are made of four compartments. The membrane potential V of each single-compartment neuron and each compartment of an IB cell follows an equation of the form :

$$C\frac{dV}{dt} = -\sum I_m - \sum I_{syn} - I_{ran}$$

where C is the membrane capacitance, I_m are the membrane currents, I_{syn} are the synaptic currents, and I_{ran} is a random input current. Some cells are also electrically coupled with gap junctions. The membrane capacitance of all neurons is equal to $0.9\mu F/cm^2$ except for VIP where it is equal to $2\mu F/cm^2$

Our regular spiking (RS) pyramidal cell model includes a leak current I_L, a sodium current I_{Na}, a potassium current I_K, and an hyperpolarization activated current (h-current) I_{AR}. There are 80 RS cells in our LIP superficial layer model, 20 in LIP granular layer, 20 in visuo-motor FEF, 20 in visual FEF and 20 in motor FEF. The 20 decision cells in visuo-motor FEF are also RS cells.

Our fast spiking (FS) interneuron model in LIP and FEF includes a leak current I_L, a sodium current I_{Na}, and a potassium current I_K. There are 20 FS cells in the LIP superficial layer, LIP granular layer and visual FEF model.

Our SOM cells model includes a leak current I_L, a sodium current I_{Na}, a potassium current I_K, and an h-current I_{AR}. There are 20 SOM cells in the LIP superficial layer, LIP deep layer, visuo-motor and visual FEF model.

Our VIP cells model includes a leak current I_L, a sodium current I_{Na}, a potassium current I_K and a potassium D-current I_D. There are 20 VIP cells in the FEF visuo-motor and FEF visual models.

Our IB cells model is made of a somatic compartment, an axonal compartment, an apical dendrite compartment and a basal dendrite compartment, with electrical coupling between them. All compartments includes a leak current I_L, a sodium current I_{Na}, and a potassium current I_K. The axonal compartment and both dendritic compartment also include a potassium M current (I_{KM}). Additionally, the apical and basal dendritic compartments include an h-current I_{AR} and a high-threshold calcium current I_{CaH}. There are 20 IB cells in the LIP model.

Each membrane channel has its membrane current I expressed in the form :

$$I = g \cdot m^p \cdot h^q \cdot (V - E)$$

where g is the channel conductance, E its reversal potential, and m and h the gating variables which follow the differential equation :

$$\frac{dx}{dt} = \frac{1}{\tau_x} \cdot (x_\infty - x), x \in \{m, h\}$$

or, in an equivalent manner :

$$\frac{dx}{dt} = \alpha_x(V) \cdot (1 - x) - \beta_x \cdot x, x \in \{m, h\}$$

Channel	$g\ (mS/cm^2)$	$E\ (mV)$	p	q	τ_m (ms)	m_∞	τ_h (ms)	h_∞
L	1	-70	0	0	-	-	-	-
Na	200	50	3	1	-	$\frac{1}{1+e^{\frac{-V-34.5}{10}}}$	$0.15+\frac{1.15}{1+e^{\frac{V+33.5}{15}}}$	$\frac{1}{1+e^{\frac{V+59.4}{10.7}}}$
K	20	-95	4	0	$0.25+4.35\cdot e^{-\frac{\lvert V+10\rvert}{10}}$	$\frac{1}{1+e^{\frac{-V-29.5}{10}}}$	-	-
h	25	-35	1	0	$\frac{1}{e^{-14.6-0.086V}+e^{-1.87+0.07V}}$	$\frac{1}{1+e^{\frac{V+87.5}{5.5}}}$	-	-

Table 1. Ion channel parameters for RS cells

Channel	$g\ (mS/cm^2)$	$E\ (mV)$	p	q	τ_m	m_∞	τ_h	h_∞
L	1	-65	0	0	-	-	-	-
Na	200	50	3	1	-	$\frac{1}{1+e^{\frac{-V-38}{10}}}$	$0.225+\frac{1.125}{1+e^{\frac{V+37}{15}}}$	$\frac{1}{1+e^{\frac{V+58.3}{6.7}}}$
K	20	-100	4	0	$0.25+4.35e^{-\frac{\lvert V+10\rvert}{10}}$	$\frac{1}{1+e^{\frac{-V-27}{11.5}}}$	-	-

Table 2. Ion channel parameters for FS cells

with the exception of the sodium currents for which $m = m_\infty(V)$.

The expressions and values for the variables and parameters g, E, p, q, τ_m and m_∞ (or α_m and β_m), τ_h and h_∞ (or α_h and β_h) for each channel and each cell types are detailed in Tables 1, 2, 3, 4 and 5.

The random current I_{ran} received by each cell follows the equation:

$$I_{ran} = \sigma_{ran}^2 \cdot dW$$

where dW is Gaussian white noise of unit variance per ms, and σ_{ran}^2 is the intensity of this additive white noise. The value of the parameter σ_{ran}^2 used for each cell type is given in Table 6.

Network connectivity

The neurons in our model interact with each other through AMPA and GABA-A synapses as well as gap junctions.

The synaptic current I_{syn} received by each cell (or compartment) is the sum of the synaptic currents $I_{syn,i}$, one for each incoming synapse. The contribution of each synapse is given by the equation:

$$I_{syn,i} = s_i \cdot g_i \cdot (V - E_i)$$

where g_i is the maximum conductance of the synapse, E_i is its reversal potential. Its synaptic gating variable s_i depends on the rise and decay time constants of the synapse $\tau_{r,i}$ and $\tau_{d,i}$ as well as the membrane potential of the presynaptic neuron $V_{pre,i}$, following the equation :

$$s_i = -\frac{s_i}{\tau_{d,i}} + \frac{1-s_i}{\tau_{r,i}} \cdot 0.5\left(1 + tanh\frac{V_{pre,i}}{10}\right)$$

Channel	$g\ (mS/cm^2)$	$E\ (mV)$	p	q	τ_m	m_∞	τ_h	h_∞
L	6	-65	0	0	-	-	-	-
Na	200	50	3	1	-	$\frac{1}{1+e^{\frac{-V-38}{10}}}$	$0.225+\frac{1.125}{1+e^{\frac{V+37}{15}}}$	$\frac{1}{1+e^{\frac{V+58.3}{6.7}}}$
K	10	-100	4	0	$0.25+4.35\cdot e^{-\frac{\lvert V+10\rvert}{10}}$	$\frac{1}{1+e^{\frac{-V-27}{11.5}}}$	-	-
h	50	-35	1	0	$\frac{1}{e^{-14.6-0.086V}+e^{-1.87+0.07V}}$	$\frac{1}{1+e^{\frac{V+75*mV}{5.5}}}$	-	-

Table 3. Ion channel parameters for SOM cells

Channel	$g\ (mS/cm^2)$	$E\ (mV)$	p	q	τ_m	m_∞	τ_h	h_∞
L	0.25	-70	0	0	-	-	-	-
Na	112.5	50	3	1	-	$\frac{1}{1+e^{-\frac{V+24}{11.5}}}$	$0.5+\frac{14}{1+e^{\frac{V+60}{12}}}$	$\frac{1}{1+e^{\frac{V+58.3}{6.7}}}$
K	225	-90	4	0	$\left(0.087+\frac{11.4}{1+e^{\frac{V+14.6}{8.6}}}\right)\cdot\left(0.087+\frac{11.4}{1+e^{-\frac{V-1.3}{18.7}}}\right)$	$\frac{1}{1+e^{-\frac{V+12.4}{6.8}}}$	-	-
D	4	-90	3	1	2	$\frac{1}{1+e^{-\frac{V+50}{20}}}$	150	$\frac{1}{1+e^{\frac{V+70}{6}}}$

Table 4. Ion channel parameters for VIP cells

Channel	$g\ (mS/cm^2)$	$E\ (mV)$	p	q	τ_m	m_∞	τ_h	h_∞
L	2 (a.d., b.d.) 1 (soma) 0.25 (axon)	-70	0	0	-	-	-	-
Na	125 (a.d., b.d.) 50 (soma) 100 (axon)	50	3	1	-	$\frac{1}{1+e^{\frac{-V-34.5}{10}}}$	$0.15+\frac{1.15}{1+e^{\frac{V+33.5}{15}}}$	$\frac{1}{1+e^{\frac{V+59.4}{10.7}}}$
K	10 (a.d., b.d., soma) 5 (axon)	-95	4	0	$0.25+4.35\cdot e^{-\frac{\lvert V+10*mV\rvert}{10}}$	$\frac{1}{1+e^{\frac{-V-29.5}{10}}}$	-	-
h	155 (a.d.) 115 (b.d)	-25	1	0	$\frac{1}{e^{-14.6-0.086V}+e^{-1.87+0.07V}}$	$\frac{1}{1+e^{\frac{V+75}{5.5}}}$	-	-
Channel	$g\ (mS/cm^2)$	$E\ (mV)$	p	q	α_m	β_m	α_h	β_h
M	0.75 (a.d., b.d) 1.5 (axon)	-95	1	0	$\frac{0.02}{1+e^{\frac{-V-20}{5}}}$	$0.01\cdot e^{\frac{-V-43}{18}}$	-	-
CaH	6.5 (a.d, b.d)	125	2	0	$\frac{1.6}{1+e^{-0.072\cdot(-V-5)}}$	$0.02\cdot\frac{V+8.9}{e^{\frac{V+8.9}{5}}-1}$	-	-

Table 5. Ion channel parameters for IB cells

Cell Type	Noise amplitude $\sigma^2_{ran}\ (mA/cm^2)$
RS	0.075
FS	0.025
SOM	0.025
VIP	0
IB (axon)	0.0125
IB (soma)	0
IB (apical dendrites)	0.0025
IB (basal dendrites)	0.0025

Table 6. Random input amplitude for each cell type

Synapse type	Source neuron	E_i	$\tau_{r,i}$	$\tau_{d,i}$
AMPA	RS, IB	0mV	0.125ms	1ms
NMDA	RS	0mV	12.5ms	125ms
GABA (fast inhibition)	FS	-80mV*	0.25ms	5ms
GABA (slow inhibition)	SOM, SI, VIP	-80mV	0.25ms	20ms

Table 7. Synaptic reversal potentials and time constants for each synapse type in the network. **FS to FS synapses have a -75mV reversal potential, instead of -80mV.*

Source region		LIP							FEF vm			FEF v			
Neuron		RS	FS	SI	g.RS	g.FS	IB	d.SI	RS	SOM	VIP	RS	FS	SOM	VIP
Target region	Neuron														
LIP	RS	-	6.25	2	2	0.1	-	-	-	-	-	-	-	-	-
	FS	0.025	2	0.2	0.1	-	0.08	-	-	-	-	-	-	-	-
	SI	0.225	0.4	7	-	-	0.045	-	-	-	-	-	-	-	-
	g.RS	-	-	-	0.5	1	-	-	-	-	-	-	-	-	-
	g.FS	-	-	-	1	0.3	-	1	-	-	-	-	-	-	-
	IB	1/60*	-	0.4	-	-	1/500	10	-	-	-	-	-	-	-
	d.SI	-	-	-	-	-	-	-	0.05	-	-	-	-	-	-
FEF vm	RS	0.009	-	-	-	-	-	-	0.6	0.5	-	-	-	-	-
	SOM	0.009	-	-	-	-	-	-	0.5	0.2	1	-	-	-	-
	VIP	-	-	-	-	-	-	-	-	-	-	-	-	-	-
FEF v	RS	0.015	-	-	-	-	-	-	-	-	-	0.2	0.2	1	-
	FS	-	-	-	-	-	-	-	-	-	-	0.2	0.2	-	-
	SOM	0.025	-	-	-	-	-	-	-	-	-	-	-	-	0.7
	VIP	0.005	-	-	-	-	-	-	-	-	-	-	-	0.01	-
FEF m	RS	-	-	-	-	-	-	-	0.1**	-	-	0.08***	-	-	-

Table 8. Maximum conductances of the synapses in the network (in mS/cm^2). **For AMPA synapse. For NMDA :* $g_i = 1/240$. ***For AMPA synapse. For NMDA :* $g_i = 0.01$. ****For NMDA synapse. For AMPA :* $g_i = 0$.

Source compartment	Target Compartment	g (mS/cm^2)
Soma	Apical Dendrite	0.2
Soma	Basal Dendrite	0.2
Soma	Axon	0.3
Apical Dendrite	Soma	0.4
Basal Dendrite	Soma	0.4
Axon Dendrite	Soma	0.3

Table 9. Conductances of gap junctions between IB cell compartments.

The parameters chosen for each type of synapse in the network are summed up in tables 7 (for the reversal potentials, rise and decay time constants) and 8 (for the maximum conductances).

Similarly, the total gap junction current received by a cell I_{gap} is the sum of all contributions $I_{gap,i}$ received from each individual cells or compartments contacting it, described by the equation :

$$I_{gap,i} = g_i \cdot (V - V_{pre,i})$$

where g_i is the maximum conductance of the gap junction and $V_{pre,i}$ is the membrane potential of the other neuron or compartment involved in the gap junction. Gap junctions are present between LIP superficial RS cells with a maximum conductance $g_i = 0.04$, between LIP superficial SI cells with a maximum conductance $g_i = 0.2$, between LIP IB cells axons with a maximum conductance $g_i = 0.0025$ and between the different compartments of each LIP IB cells, with conductances summed up in Table 9.

Finally, some cell populations in the network receive an external input current I_{inp}, following the set of equations :

$$I_{inp} = s_{inp} \cdot g_{inp} \cdot (V - E_{inp})$$
$$\frac{ds_{inp}}{dt} = -\frac{s_{inp}}{\tau_{d,inp}} + \frac{(1 - s_{inp})}{\tau_{r,inp}} \cdot 0.5 \left(1 + tanh\frac{V_{inp}}{10}\right)$$

Parameter	mdPul input	LIP input (only when FEF is modeled alone)	FEF input (only when LIP is modeled alone)	V4 input (only during target appearance)
Good theta f	13Hz	50Hz	25Hz	50Hz
Poor theta f	-	13Hz	-	50Hz
g_{inp}	to LIP gran. RS : 5 to LIP gran. FS : 5 to FEF vm VIP : 10	to FEF vm RS : 3 to FEF vm SOM : 3 to FEF v VIP : 2.5 to FEF v SOM : 7.5 to FEF v RS : 7.5	to LIP deep SI : 5	to FEF v VIP : 3 to FEF v SOM : 2.5

Table 10. Nominal frequency and maximum conductances (in mS/cm^2) of inputs to the model, coming from mdPul, LIP, FEF or V4.

where g_{inp} is the maximum conductance of the input synapse, $E_{inp} = 0mV$ is its reversal potential. Its synaptic gating variable s_{inp} depends on the rise and decay time constants of the synapse $\tau_{r,inp} = 0.1ms$ and $\tau_{d,inp} = 0.5ms$ as well as the membrane potential of the presynaptic neuron V_{inp}.

Input neurons are not modeled explicitly, but instead their spike trains are predetermined, and whenever a spike occurs, their membrane potential is set to $V_{inp} = V_{high} = 0mV$ before exponentially decaying to its baseline value $V_{inp} = V_{low} = -80mV$ with a decay time constant $\tau_{inp} = 0.5ms$:

$$\frac{dV_{inp}}{dt} = \frac{1}{\tau_{inp}} \cdot (V_{low} - V_{inp})$$
$$\text{on spike} : V_{inp} \leftarrow V_{high}$$

When the input is periodic with frequency f, the time between two pulses is a random number, uniformly distributed in the interval $(0.9f, 1.1f)$, chosen independently for each input neuron. The frequency f and conductance g_{inp} for each input synapse are given in Table 10.

Simulation tools

All the simulations were performed using the Brian2 libraries for Python (see ***Stimberg et al.*** (***2014***)), using a 4th order Runge-Kutta method to solve the differential equations defining the model, and a 0.01ms timestep.

Statistical analysis

All analyses were performed in Python. LIP LFPs were computed by averaging the membrane potentials of superficial RS cells, while FEF visuo-motor LFPs were computed by averaging the membrane potentials of visuo-motor RS cells.

Funding Information

This research has been supported by funding from the NIH/NIMH grant P50 MH109429 on Neurobiology and Dynamics of Active Sensing.

References

Audette NJ, Urban-Ciecko J, Matsushita M, Barth AL. POm Thalamocortical Input Drives Layer-Specific Microcircuits in Somatosensory Cortex. Cerebral Cortex. 2018; 28(4):1312–1328. https://doi.org/10.1093/cercor/bhx044, doi: 10.1093/cercor/bhx044.

Benedetto A, Morrone MC, Tomassini A. The Common Rhythm of Action and Perception. Journal of Cognitive Neuroscience. 2020 Feb; 32(2):187–200. https://doi.org/10.1162/jocn_a_01436, doi: 10.1162/jocn_a_01436.

Bisley JW, Mirpour K, Arcizet F, Ong WS. The role of the lateral intraparietal area in orienting attention and its implications for visual search. European Journal of Neuroscience. 2011 Jun; 33(11):1982–1990. https://doi.org/10.1111/j.1460-9568.2011.07700.x, doi: 10.1111/j.1460-9568.2011.07700.x.

Buschman TJ, Miller EK. Top-Down Versus Bottom-Up Control of Attention in the Prefrontal and Posterior Parietal Cortices. Science. 2007 Mar; 315(5820):1860–1862. https://doi.org/10.1126/science.1138071, doi: 10.1126/science.1138071.

Corbetta M, Akbudak E, Conturo TE, Snyder AZ, Ollinger JM, Drury HA, Linenweber MR, Petersen SE, Raichle ME, Essen DCV, Shulman GL. A Common Network of Functional Areas for Attention and Eye Movements. Neuron. 1998 Oct; 21(4):761–773. https://doi.org/10.1016/s0896-6273(00)80593-0, doi: 10.1016/s0896-6273(00)80593-0.

Cruikshank SJ, Urabe H, Nurmikko AV, Connors BW. Pathway-Specific Feedforward Circuits between Thalamus and Neocortex Revealed by Selective Optical Stimulation of Axons. Neuron. 2010 Jan; 65(2):230–245. https://doi.org/10.1016/j.neuron.2009.12.025, doi: 10.1016/j.neuron.2009.12.025.

Fiebelkorn IC, Kastner S. The Puzzling Pulvinar. Neuron. 2019 Jan; 101(2):201–203. https://doi.org/10.1016/j.neuron.2018.12.032, doi: 10.1016/j.neuron.2018.12.032.

Fiebelkorn IC, Kastner S. A Rhythmic Theory of Attention. Trends in Cognitive Sciences. 2019 Feb; 23(2):87–101. https://doi.org/10.1016/j.tics.2018.11.009, doi: 10.1016/j.tics.2018.11.009.

Fiebelkorn IC, Pinsk MA, Kastner S. A Dynamic Interplay within the Frontoparietal Network Underlies Rhythmic Spatial Attention. Neuron. 2018 Aug; 99(4):842–853.e8. https://doi.org/10.1016/j.neuron.2018.07.038, doi: 10.1016/j.neuron.2018.07.038.

Fiebelkorn IC, Pinsk MA, Kastner S. The mediodorsal pulvinar coordinates the macaque fronto-parietal network during rhythmic spatial attention. Nature Communications. 2019 Jan; 10(1). https://doi.org/10.1038/s41467-018-08151-4, doi: 10.1038/s41467-018-08151-4.

Fiebelkorn IC, Saalmann YB, Kastner S. Rhythmic Sampling within and between Objects despite Sustained Attention at a Cued Location. Current Biology. 2013 Dec; 23(24):2553–2558. https://doi.org/10.1016/j.cub.2013.10.063, doi: 10.1016/j.cub.2013.10.063.

Fries P. Neuronal Gamma-Band Synchronization as a Fundamental Process in Cortical Computation. Annual Review of Neuroscience. 2009 Jun; 32(1):209–224. https://doi.org/10.1146/annurev.neuro.051508.135603, doi: 10.1146/annurev.neuro.051508.135603.

Gaillard C, Hassen SBH, Bello FD, Bihan-Poudec Y, VanRullen R, Hamed SB. Prefrontal attentional saccades explore space rhythmically. Nature Communications. 2020 Feb; 11(1). https://doi.org/10.1038/s41467-020-14649-7, doi: 10.1038/s41467-020-14649-7.

Gelastopoulos A, Whittington MA, Kopell NJ. Parietal low beta rhythm provides a dynamical substrate for a working memory buffer. Proceedings of the National Academy of Sciences. 2019 Aug; 116(33):16613–16620. https://doi.org/10.1073/pnas.1902305116, doi: 10.1073/pnas.1902305116.

Gregoriou GG, Gotts SJ, Desimone R. Cell-Type-Specific Synchronization of Neural Activity in FEF with V4 during Attention. Neuron. 2012 Feb; 73(3):581–594. https://doi.org/10.1016/j.neuron.2011.12.019, doi: 10.1016/j.neuron.2011.12.019.

Gutierrez C, Cola MG, Seltzer B, Cusick C. Neurochemical and connectional organization of the dorsal pulvinar complex in monkeys. The Journal of Comparative Neurology. 2000 Mar; 419(1):61–86. https://doi.org/10.1002/(sici)1096-9861(20000327)419:1<61::aid-cne4>3.0.co;2-i, doi: 10.1002/(sici)1096-9861(20000327)419:1<61::aid-cne4>3.0.co;2-i.

Halassa MM, Kastner S. Thalamic functions in distributed cognitive control. Nature Neuroscience. 2017 Nov; 20(12):1669–1679. https://doi.org/10.1038/s41593-017-0020-1, doi: 10.1038/s41593-017-0020-1.

Helfrich RF, Fiebelkorn IC, Szczepanski SM, Lin JJ, Parvizi J, Knight RT, Kastner S. Neural Mechanisms of Sustained Attention Are Rhythmic. Neuron. 2018 Aug; 99(4):854–865.e5. https://doi.org/10.1016/j.neuron.2018.07.032, doi: 10.1016/j.neuron.2018.07.032.

Jaramillo J, Mejias JF, Wang XJ. Engagement of Pulvino-cortical Feedforward and Feedback Pathways in Cognitive Computations. Neuron. 2019 Jan; 101(2):321–336.e9. https://doi.org/10.1016/j.neuron.2018.11.023, doi: 10.1016/j.neuron.2018.11.023.

Karnani MM, Jackson J, Ayzenshtat I, Sichani AH, Manoocheri K, Kim S, Yuste R. Opening Holes in the Blanket of Inhibition: Localized Lateral Disinhibition by VIP Interneurons. Journal of Neuroscience. 2016 Mar; 36(12):3471–3480. https://doi.org/10.1523/jneurosci.3646-15.2016, doi: 10.1523/jneurosci.3646-15.2016.

Kastner S, Fiebelkorn IC, Eradath MK. Dynamic pulvino-cortical interactions in the primate attention network. Current Opinion in Neurobiology. 2020 Dec; 65:10–19. https://doi.org/10.1016/j.conb.2020.08.002, doi: 10.1016/j.conb.2020.08.002.

Kramer MA, Roopun AK, Carracedo LM, Traub RD, Whittington MA, Kopell NJ. Rhythm Generation through Period Concatenation in Rat Somatosensory Cortex. PLoS Computational Biology. 2008 Sep; 4(9):e1000169. https://doi.org/10.1371/journal.pcbi.1000169, doi: 10.1371/journal.pcbi.1000169.

Landau AN, Fries P. Attention Samples Stimuli Rhythmically. Current Biology. 2012 Jun; 22(11):1000–1004. https://doi.org/10.1016/j.cub.2012.03.054, doi: 10.1016/j.cub.2012.03.054.

Lee JH, Whittington MA, Kopell NJ. Top-Down Beta Rhythms Support Selective Attention via Interlaminar Interaction: A Model. PLoS Computational Biology. 2013 Aug; 9(8):e1003164. https://doi.org/10.1371/journal.pcbi.1003164, doi: 10.1371/journal.pcbi.1003164.

Miller EK, Buschman TJ. Cortical circuits for the control of attention. Current Opinion in Neurobiology. 2013 Apr; 23(2):216–222. https://doi.org/10.1016/j.conb.2012.11.011, doi: 10.1016/j.conb.2012.11.011.

Moore T, Fallah M. Control of eye movements and spatial attention. Proceedings of the National Academy of Sciences. 2001 Jan; 98(3):1273–1276. https://doi.org/10.1073/pnas.98.3.1273, doi: 10.1073/pnas.98.3.1273.

Pogosyan A, Gaynor LD, Eusebio A, Brown P. Boosting Cortical Activity at Beta-Band Frequencies Slows Movement in Humans. Current Biology. 2009 Oct; 19(19):1637–1641. https://doi.org/10.1016/j.cub.2009.07.074, doi: 10.1016/j.cub.2009.07.074.

Romanski LM, Giguere M, Bates JF, Goldman-Rakic PS. Topographic organization of medial pulvinar connections with the prefrontal cortex in the rhesus monkey. The Journal of Comparative Neurology. 1997 Mar; 379(3):313–332. https://doi.org/10.1002/(sici)1096-9861(19970317)379:3<313::aid-cne1>3.0.co;2-6, doi: 10.1002/(sici)1096-9861(19970317)379:3<313::aid-cne1>3.0.co;2-6.

Roopun AK, Kramer MA, Carracedo LM, Kaiser M, Davies CH, Traub RD, Kopell NJ, Whittington MA. Period concatenation underlies interactions between gamma and beta rhythms in neocortex. Frontiers in Cellular Neuroscience. 2008; 2. https://doi.org/10.3389/neuro.03.001.2008, doi: 10.3389/neuro.03.001.2008.

Saalmann YB, Kastner S. Cognitive and Perceptual Functions of the Visual Thalamus. Neuron. 2011 Jul; 71(2):209–223. https://doi.org/10.1016/j.neuron.2011.06.027, doi: 10.1016/j.neuron.2011.06.027.

Selemon L, Goldman-Rakic P. Common cortical and subcortical targets of the dorsolateral prefrontal and posterior parietal cortices in the rhesus monkey: evidence for a distributed neural network subserving spatially guided behavior. The Journal of Neuroscience. 1988 Nov; 8(11):4049–4068. https://doi.org/10.1523/jneurosci.08-11-04049.1988, doi: 10.1523/jneurosci.08-11-04049.1988.

Song K, Meng M, Chen L, Zhou K, Luo H. Behavioral Oscillations in Attention: Rhythmic α Pulses Mediated through θ Band. The Journal of Neuroscience. 2014 Apr; 34(14):4837–4844. https://doi.org/10.1523/jneurosci.4856-13.2014, doi: 10.1523/jneurosci.4856-13.2014.

Stimberg M, Goodman DF, Benichoux V, Brette R. Equation-oriented specification of neural models for simulations. Frontiers in Neuroinformatics. 2014; 8.

Tremblay R, Lee S, Rudy B. GABAergic Interneurons in the Neocortex: From Cellular Properties to Circuits. Neuron. 2016 Jul; 91(2):260–292. https://doi.org/10.1016/j.neuron.2016.06.033, doi: 10.1016/j.neuron.2016.06.033.

VanRullen R, Carlson T, Cavanagh P. The blinking spotlight of attention. Proceedings of the National Academy of Sciences. 2007 Nov; 104(49):19204–19209. https://doi.org/10.1073/pnas.0707316104, doi: 10.1073/pnas.0707316104.

Zhang S, Xu M, Kamigaki T, Do JPH, Chang WC, Jenvay S, Miyamichi K, Luo L, Dan Y. Long-range and local circuits for top-down modulation of visual cortex processing. Science. 2014 Aug; 345(6197):660–665. https://doi.org/10.1126/science.1254126, doi: 10.1126/science.1254126.

Zhang Y, Chen Y, Bressler SL, Ding M. Response preparation and inhibition: The role of the cortical sensorimotor beta rhythm. Neuroscience. 2008 Sep; 156(1):238–246. https://doi.org/10.1016/j.neuroscience.2008.06.061, doi: 10.1016/j.neuroscience.2008.06.061.

Zhou H, Schafer RJ, Desimone R. Pulvinar-Cortex Interactions in Vision and Attention. Neuron. 2016 Jan; 89(1):209–220. https://doi.org/10.1016/j.neuron.2015.11.034, doi: 10.1016/j.neuron.2015.11.034.

Zhou N, Masterson SP, Damron JK, Guido W, Bickford ME. The Mouse Pulvinar Nucleus Links the Lateral Extrastriate Cortex, Striatum, and Amygdala. The Journal of Neuroscience. 2018 Jan; 38(2):347–362. https://doi.org/10.1523/jneurosci.1279-17.2017, doi: 10.1523/jneurosci.1279-17.2017.

Appendix

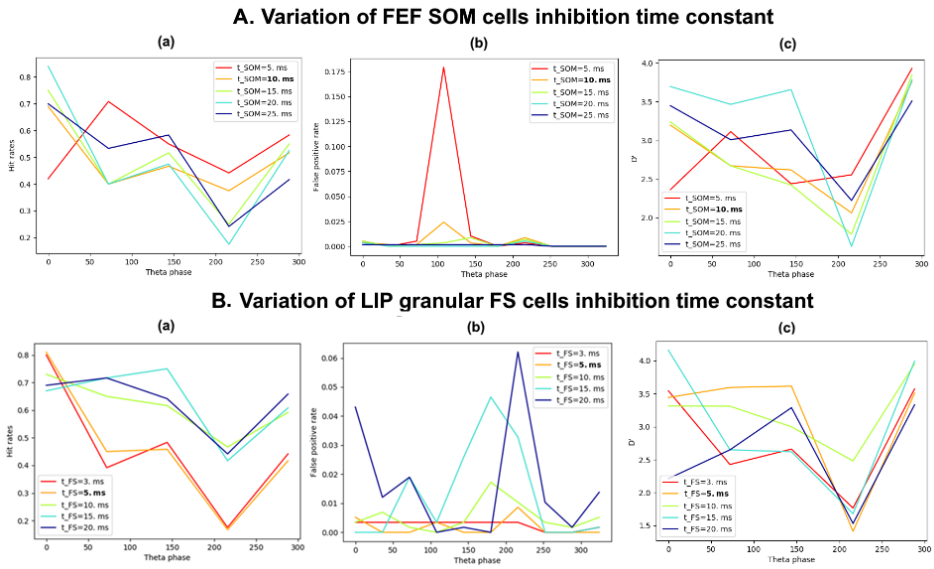

Figure S1. Changing FEF and LIP oscillatory frequency negatively impacts task performance. A. Effect of the variation of FEF rhythm (a) hit rates as function of the θ phase, with different values of the FEF SOM cells inhibition time constant. (b) false alarm rate as function of the θ phase, with different values of the FEF SOM cells inhibition time constant. (c) D' measure as function of the θ phase, with different values of the FEF SOM cells inhibition time constant. B. Effect of the variation of LIP rhythm (a) hit rates as function of the θ phase, with different values of the LIP FS cells inhibition time constant. (b) false alarm rate as function of the θ phase, with different values of the LIP FS cells inhibition time constant. (c) D' measure as function of the θ phase, with different values of the LIP FS cells inhibition time constant.

Influence of Tonic Excitation on LIP Behavior

The tonic excitation range for the LIP module to exhibit behavior matching experimental observations is rather broad (between -7 and 2uA/cm^2 for FS cells and between -25 and 15 uA/cm^2 for RS cells), but choosing excitation levels out of this range can disturb both the beta1 rhythm during poor theta phase and the gamma rhythm during good theta phase. Excessive tonic excitation of input layer FS cells – which inhibit superficial RS cells (see LIP model, Figure 4-A) – disturbs the beta1 rhythm by preventing superficial RS cell spiking (Figure S6-A), while insufficient tonic drive to input layer FS cells disturbs the beta1 rhythm by allowing input RS cells to spike and entrain the superficial layer (Figure S6-B). Finally, insufficient tonic excitation to input layer RS cells disturbs the good theta phase gamma rhythm, rendering RS cells unable to sustain their activity outside the windows of disinhibition provided by deep SOM cells spiking (Figure S6-C).

Influence of Input Parameters on FEF Visuo-Motor Module Behavior

Our explorations indicate that a broad range of tonic excitation levels result in RS cell quiescence during the poor theta phase and beta2 rhythmicity in RS and SOM cells during the good theta phase (S8). Too much tonic excitation to RS cells compared to SOM cells (Figure S8-A) results in RS cell firing during the poor theta phase despite SOM cell inhibition, while too little tonic excitation to RS cells compared to SOM cells results in the RS cells being unable to take control of SOM cells outside of the windows of disinhibition provided by VIP cells in the good theta phase, and a resulting beta1 (rather than beta2) rhythm.

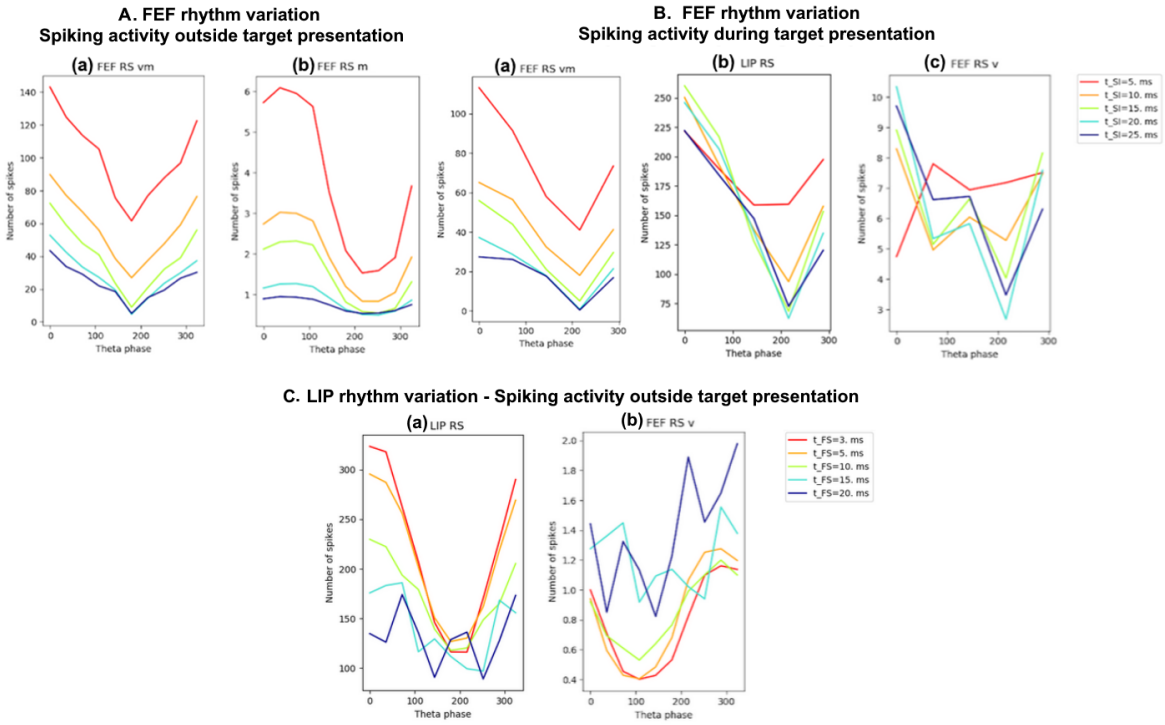

Figure S2. A. Increasing FEF visuo-motor cells oscillatory frequency leads to higher false alarm rates in good θ phase, but not in poor θ phase. (a)(b) Number of spikes in 125ms-long windows outside target presentation in FEF visuo-motor cells and FEF decision cells respectively, as function of the θ phase. **B. Increasing FEF visuo-motor cells oscillatory frequency leads to higher hit rates in the poor θ phase, and lower hit rates in the good θ phase.** (a)(b)(c) Number of spikes during target presentation in FEF visuo-motor cells, LIP superficial RS cells and FEF visual cells respectively, as function of the θ phase. **C. Reducing LIP oscillatory frequency leads to higher hit rates and false alarm rates.** (a)(b) Number of spikes in 125ms-long windows outside target presentation in LIP superficial RS cells and FEF visual cells respectively, as function of the θ phase.

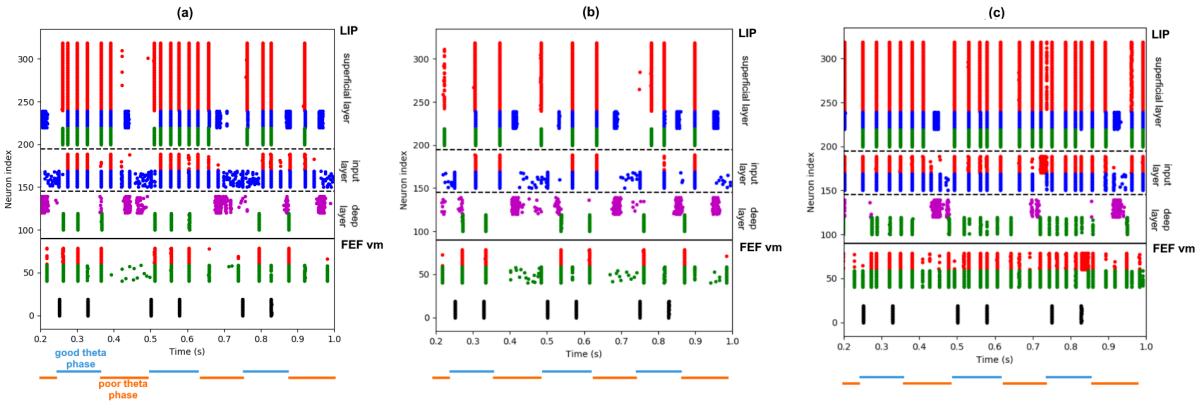

Figure S3. Reducing FEF visuo-motor SOM cells time constant and increasing LIP granular FS cells time constants have distinct effect on LIP oscillations (a) Raster plot of LIP and FEF visuo-motor module in a 1-second simulation of attention network with unchanged inhibition time constants. (b) Raster plot of LIP and FEF visuo-motor module in a 1-second simulation of attention network with LIP granular FS cells time constant set to 20ms, showing more beta oscillations. (c) Raster plot of LIP and FEF visuo-motor module in a 1-second simulation of attention network with FEF visuo-motor SOM cells time constant set to 5ms, showing more γ oscillations.

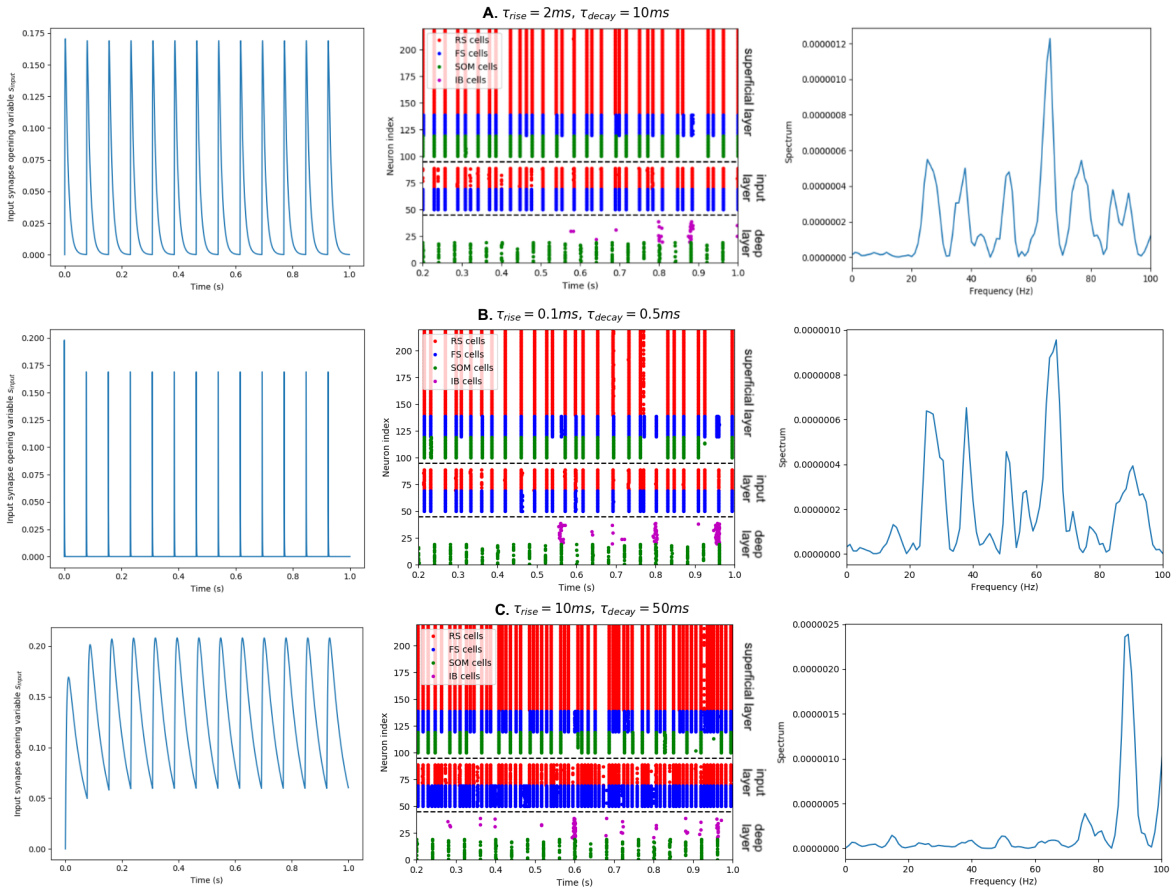

Figure S4. LIP good θ phase γ can be obtained with mdPul α stimulation of various widths. A. LIP good θ phase behavior with mdPul input synapse timescales of $\tau_{rise} = 2ms$ and $\tau_{decay} = 10ms$, the default values used throughout this paper (left: input synapse opening variable of a 1s-long simulation, middle: Raster plot of a 1s-long simulation, right: power spectrum of the LFP generated by the network in this 1s-long simulation). B. LIP good θ phase behavior with shorter mdPul input synapse timescales of $\tau_{rise} = 0.1ms$ and $\tau_{decay} = 0.5ms$ (left: input synapse opening variable of a 1s-long simulation, middle: Raster plot of a 1s-long simulation, right: power spectrum of the LFP generated by the network in this 1s-long simulation). C. LIP good θ phase behavior with longer mdPul input synapse timescales of $\tau_{rise} = 10ms$ and $\tau_{decay} = 50ms$ (left: input synapse opening variable of a 1s-long simulation, middle: Raster plot of a 1s-long simulation, right: power spectrum of the LFP generated by the network in this 1s-long simulation).

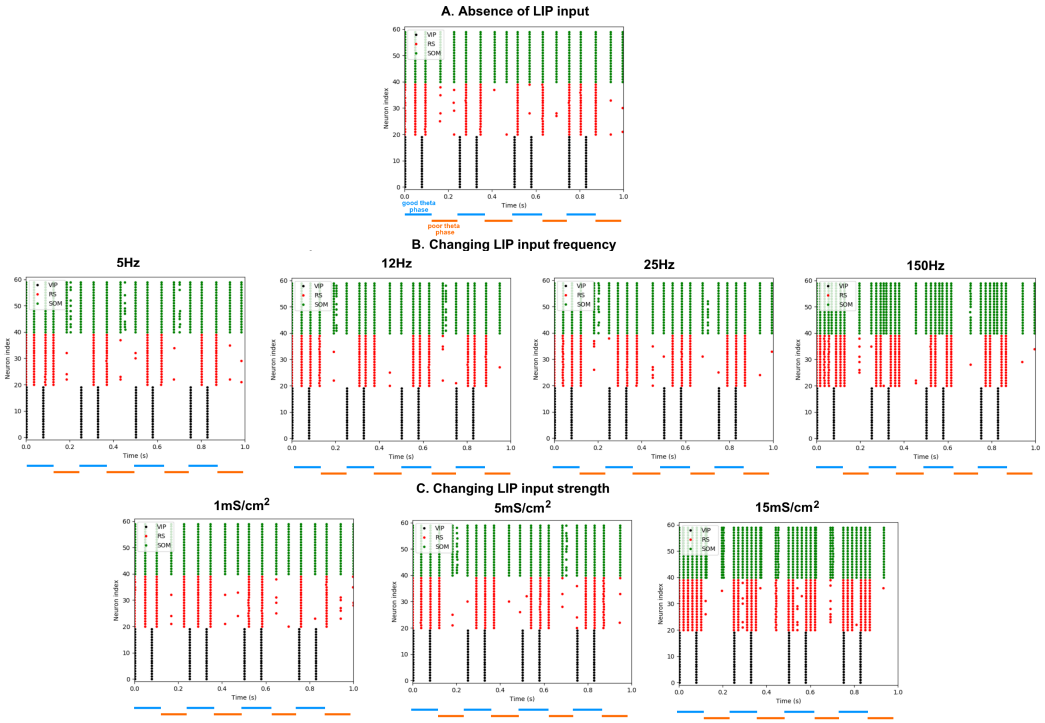

Figure S5. FEF visuo-motor module good θ phase behavior is influenced by LIP input properties A. Raster plot of FEF visuo-motor behavior without LIP input during a 1s-long simulation with alternating good and poor θ phase (the good θ phase β_2 rhythm gets slower). B. Raster plots of FEF visuo-motor behavior with various LIP input frequencies during 1s-long simulations with alternating good and poor θ phase. Top-Left: 5Hz LIP input (the good θ phase β_2 rhythm gets slower). Top-Right: 12Hz LIP input (the good θ phase β_2 rhythm gets slower). Bottom-Left: 20Hz mdPul input (the good θ phase β_2 rhythm is preserved). Bottom-Right: 150Hz mdPul input (the good θ phase β_2 rhythm gets faster). C. Raster plots of FEF visuo-motor behavior with various LIP input strengths during 1s-long simulations with alternating good and poor θ phase. Left: $2mS/cm^2$ input. Middle: $5mS/cm^2$ input. Right: $15mS/cm^2$ input.

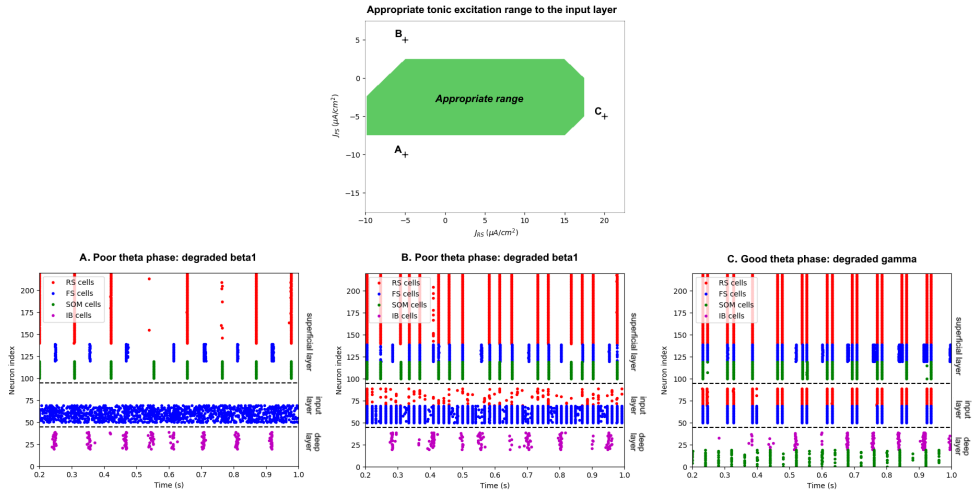

Figure S6. LIP good and poor theta phase behavior depends on input layer tonic excitation Top: Appropriate tonic excitation range needed to obtain a gamma rhythm in the good theta phase and beta1 rhythm in the poor theta phase. Bottom: A. Having excessive tonic excitation to input layer FS cells disturbs the poor theta phase beta1 rhythm by preventing superficial RS cells spikes. B. Having insufficient tonic excitation to input layer FS cells disturbs the poor theta phase beta1 rhythm by allowing input RS cells to spike and entrain the superficial layer. C. Having insufficient tonic excitation to input layer RS cells disturbs the good theta phase gamma rhythm.

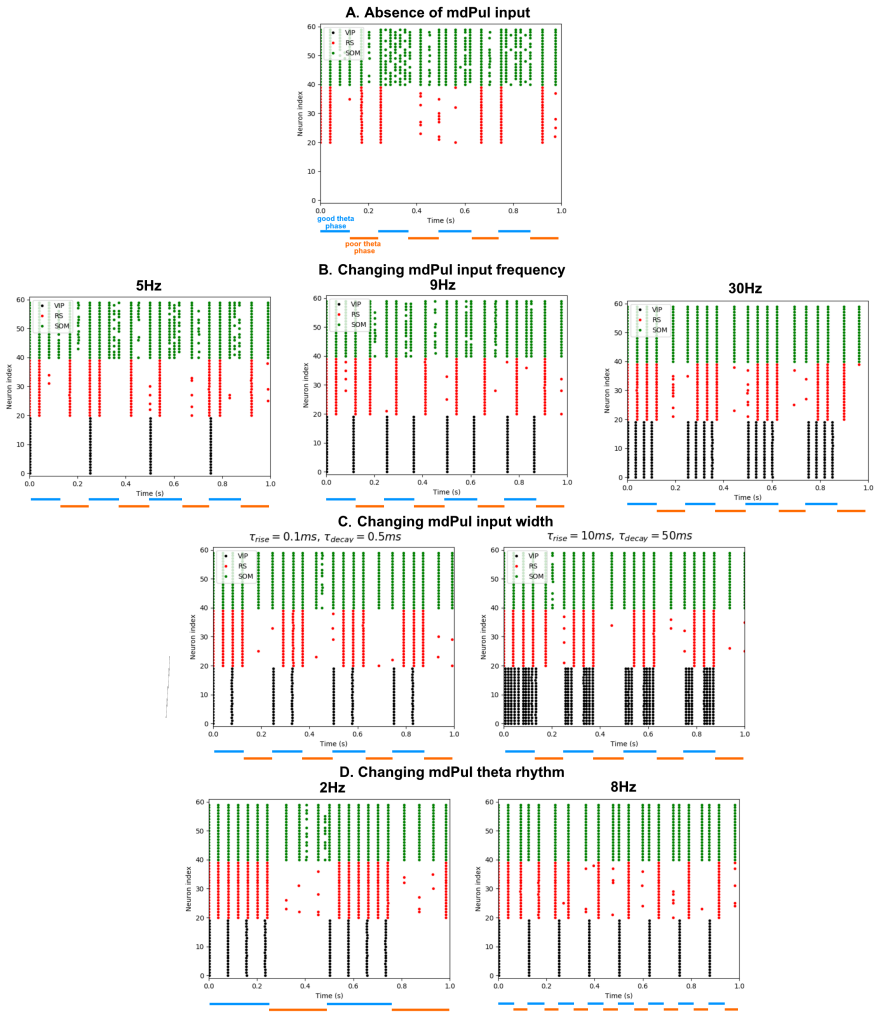

Figure S7. FEF visuo-motor module good theta phase behavior is influenced by mdPul input properties A. Raster plot of FEF visuo-motor behavior without mdPul input during a 1s-long simulation with alternating good and poor theta phase (no beta2 rhythm appears in the good theta phase). B. Raster plots of FEF visuo-motor behavior with various mdPul input frequencies, during a 1s-long simulations with alternating good and poor theta phase. Left: 5Hz mdPul input (the beta2 rhythm is not sustained). Middle: 9Hz mdPul input (the beta2 rhythm is not sustained). Right: 30Hz mdPul input (the beta2 rhythm is preserved). C. Raster plot of FEF visuo-motor good theta phase behavior with altered mdPul input synapse timescales. Left: $\tau_{rise} = 0.1ms$ and $\tau_{decay} = 0.5ms$ (the beta2 rhythm is preserved). Right: $\tau_{rise} = 10ms$ and $\tau_{decay} = 50ms$ (the beta2 rhythm is preserved). D. Raster plots of FEF visuo-motor behavior, during a 1s-long simulations with alternating good and poor theta phase with various frequencies. Left: 2Hz "theta" input (the beta2 rhythm is sustained). Right: 8Hz "theta" input (the beta2 rhythm is not sustained).

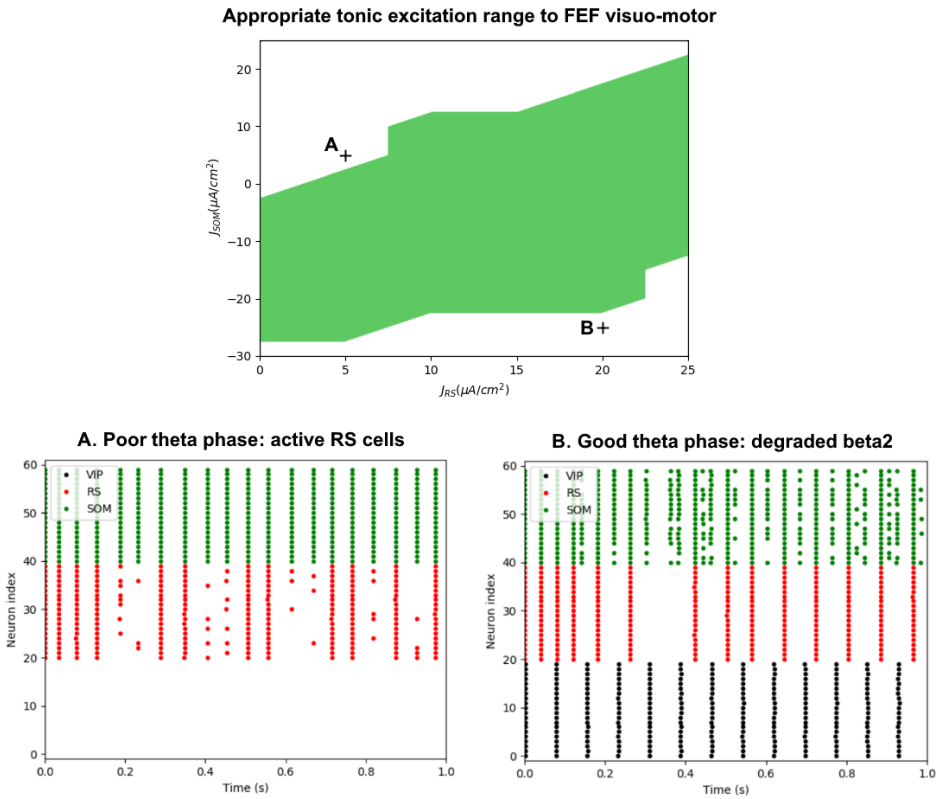

Figure S8. FEF visuo-motor module good and poor theta phase behavior depends on the tonic excitation given to RS and SOM cells Top: Appropriate tonic excitation range needed to obtain a beta2 rhythm in the good theta phase and quiet RS cells in the poor theta phase. The crosses indicate the two sets of values used in simulation A. and B. respectively. Bottom: A. Having insufficient tonic excitation to SOM cells disturbs the poor theta phase by allowing RS cells spikes. B. Having excessive tonic excitation to SOM cells disturbs the good theta phase beta2 rhythm by silencing RS cells outside the disinhibition windows provided by VIP cells.